d'ordre: XX/2025.C/GE

People's Democratic Republic of Algeria

Ministry of Higher Education and Scientific Research

University of Saida

Faculty of Mathematics, Informatics, and Telecommunications

Laboratory of Electronics,Advanced Signal Processing, and Microwave (LESM)

A Doctoral Thesis

Submitted in Fulfillment of the Requirements for Degree of Doctor (LMD)

Field: Telecommunications

Specialization: Telecommunication Devices and Systems

Performance Optimization of Fractal Multi-Band Antennas

Presented by: Abdelbasset AZZOUZ

Supervised by: Dr. Rachid Bouhmidi, Co-supervised by: Prof. Mohammed Chetioui

Defended on 07/07/2026, in the presence of the Examination Committee:

Role	**Affiliation**	**Rank**	**Name**
Chair	University of Saida	Professor	Mehdi DAMOU
Supervisor	University of Saida	MCA	Rachid Bouhmidi
Co-Supervisor	University of Saida	Professor	Mohammed Chetioui
Examiner	University of Saida	MCA	Abdelhakim Boudkhil
Examiner	Sidi BelAbbes University	Professor	Chama Zouaoui
Examiner	Sidi BelAbbes University	MCA	Berrahal Belabbes

Academic Year: 2025-2026 / 1447-1448 AH

Prophetic Hadith

The Messenger of Allah said: "Whoever follows a path in pursuit of knowledge, Allah will make easy for him a path to Paradise." — Narrated by Muslim

– Prophet Muhammad (PBUH)

Dedication

I dedicate this doctoral thesis to my grandmothers and grandfathers,
whose guidance and wisdom continue to inspire me.

I also extend my deepest gratitude and love to my parents and siblings, whose endless support gave me the strength
to persevere when things got tough.

– Abdelbasset Azzouz

Acknowledgments

I express my deepest gratitude to Almighty **ALLAH** for granting me the resilience, determination, and perseverance to undertake and successfully complete this research work.

I extend my sincere appreciation to my supervisor, Dr. Rachid Bouhmidi, and my co-supervisor, Prof. Mohammed Chetioui, for their invaluable guidance, unwavering support, and expert insights throughout the course of this project.

I am profoundly indebted to Prof. Mouloud Challal for his expert guidance and steadfast encouragement. I also greatly appreciate the valuable insights and assistance provided by Dr. Riadh Degachi, Dr. Ahmed Jamal Abdullah Al-Gburi, and Dr. Mehr E Munir, throughout my research journey.

My sincere thanks are extended to the dissertation committee, for their willingness to serve on the examining board and their thoughtful evaluations.

Finally, I express my heartfelt gratitude to my family for their unrelenting encouragement, patience, and support, which have been a constant source of motivation and strength.

– *Abdelbasset Azzouz*

Abstract

The thesis focuses on the development, optimization, and validation of compact multiband microstrip antennas based on fractal geometries for modern wireless applications. After reviewing microstrip antenna fundamentals and fractal concepts for size reduction and multiband performance, several novel designs are proposed. A hybrid wheel antenna integrating Sierpinski carpet and Koch snowflake patterns delivers five-band performance, offering both high gain and broad bandwidth. An ANN-based optimization enhances a modified Apollonian gasket antenna's return loss and impedance matching. A compact rectangular nested fractal antenna demonstrates multiband and high-gain performance across seven bands. Finally, a Python-assisted automated approach optimizes an inverted Sierpinski crossed bowtie antenna using HFSS simulations. Simulated and measured results show excellent agreement, validating the proposed methods. The study offers a systematic framework for developing efficient, high-gain, multiband fractal antennas for Wi-Fi, WLAN, satellite, radar, and 5G systems.

Keywords: Fractal antennas, Multiband antennas, Genetic algorithms, Artificial neural networks, Defected ground structure, MIMO antennas, Array antennas.

Résumé

Cette thèse présente la conception, l'optimisation et la validation d'antennes microbandes multibandes compactes basées sur des géométries fractales pour les applications sans fil modernes. Après une revue des principes fondamentaux des antennes microbandes et des concepts fractals visant la miniaturisation et le comportement multibande, plusieurs conceptions novatrices sont proposées. Une antenne hybride en forme de roue, combinant les géométries du tapis de Sierpinski et du flocon de Koch, atteint un fonctionnement à cinq bandes avec un gain élevé et une large bande passante. Une optimisation basée sur les réseaux de neurones artificiels (ANN) améliore les pertes de retour et l'adaptation d'impédance d'une antenne modifiée à motif d'Apollonius. Une antenne fractale rectangulaire imbriquée compacte démontre des performances multibandes et un gain élevé sur sept bandes. Enfin, une approche automatisée assistée par Python optimise une antenne fractale croisée de Sierpinski inversée à l'aide de simulations HFSS. Les résultats simulés et mesurés montrent un excellent accord, validant les méthodes proposées. Cette étude offre un cadre systématique pour le développement d'antennes fractales efficaces, à haut gain et multibandes adaptées aux systèmes Wi-Fi, WLAN, satellite, radar et 5G.

mots-clés: Antennes fractales, Antennes multibandes, Algorithmes génétiques, Réseaux de neurones artificiels, Structure de sol défectueuse, Antennes MIMO, Antennes en réseau.

مُلخّص

تركز هذه الأطروحة على تصميم وتحسين وتحقق هوائيات المايكروستريب متعددة النطاقات والمضغوطة، المعتمدة على الهندسات الفراكتلية للتطبيقات اللاسلكية الحديثة. بعد استعراض أساسيات هوائيات المايكروستريب ومفاهيم الفراكتل بهدف تقليل الحجم وتحقيق الأداء متعدد النطاقات، تم اقتراح عدة تصاميم مبتكرة. يحقق الهوائي الهجين على شكل عجلة، الذي يجمع بين هندستي سجادة سيربينسكي وندفة الثلج لكوخ، تشغيلًا في خمس نطاقات مع كسب عالٍ وعرض نطاق واسع. كما تعمل خوارزمية التحسين المعتمدة على الشبكات العصبية الاصطناعية على تحسين فقد الإنعكاس وتطابق المانعة لهوائي معدل يعتمد على شكل أبولونيان. وتم أيضًا تطوير هوائي فراكتلي مستطيل مدمج ومتحقق تجريبيًا، أظهر أداءً متعدد النطاقات وكسبًا مرتفعًا عبر سبعة نطاقات ترددية. وأخيرًا، تم تقديم نهج آلي للتصميم والتحسين باستخدام بايثون لنموذج هوائي سيربينسكي المعكوس المتقاطع، بالاعتماد على محاكاة حذصص. أظهرت النتائج توافقًا ممتازًا بين المحاكاة والقياسات، مما يؤكد فعالية الأساليب المقترحة. وتقدم هذه الدراسة إطارًا منهجيًا لتطوير هوائيات فراكتلية فعّالة، عالية الكسب ومتعددة النطاقات، مناسبة لتطبيقات واذ وواا والأقمار الصناعية والرادار وأنظمة الجيل الخامس (٥ج).

الكلمات المفتاحيّة: هوائيات الفراكتال، هوائيات متعددة النطاقات، الخوارزميات الجينية، الشبكات العصبية الاصطناعية، الهيكل الأرضي المتخلخل، هوائيات پيپو، هوائيات المصفوفة.

Table of Contents

List of Figures

List of Tables

CHAPTER 1

Introduction and Microstrip Antenna Overview

1 Introduction

1.1 Motivation

In the era of rapid technological advancement, wireless communication systems have become essential in both personal and professional domains. Devices such as smartphones, tablets, laptops, satellite communication systems, and RFID units are becoming increasingly compact, yet are expected to deliver high-speed, reliable, and uninterrupted connectivity across multiple communication standards. Significant design issues are imposed by this trend of shrinking, particularly for the antenna, It is among the most crucial components of any wireless system. For electromagnetic signals to be transmitted and received effectively, antennas are necessary. Their performance directly affects the quality and extent of communication.

Traditionally, an antenna's resonant wavelength is directly correlated with its physical size. Thus, operating at lower frequencies typically necessitates larger antenna sizes, which contradicts the modern demand for miniaturized and portable devices. Additionally, with the explosion of various wireless standards such as GSM, LTE, Wi-Fi, Bluetooth, Zigbee, WiMAX, and upcoming 5G/6G technologies spanning frequencies from below 1 GHz to above 10 GHz, It is becoming more and more important to have antennas that can operate efficiently across a range of frequency bands. Compact platform integration is made easier by multiband operation, which eliminates the need for several antennas.

Microstrip patch antennas are regarded as excellent options for such applications due to its lightweight, conformable, low-profile design, ease of manufacturing, and compatibility with printed circuit board technology. However, their limited gain and narrow bandwidth are intrinsic problems. To address these issues, a number of strategies have been devised, such as the usage of metamaterials, electromagnetic band gap (EBG) structures, defected ground structures (DGS), and slots. Among these, the application of fractal geometries has demonstrated great promise. The self-similarity and space-filling properties of fractals allow for multiband behavior and shrinking without compromising antenna performance. Additionally, artificial intelligence (AI) has become a potent tool for antenna design and optimization, especially artificial neural networks (ANNs). Conventional design techniques need parametric sweeps and lengthy simulations, which are computationally costly and time-consuming. AI-based models can greatly speed up the development process by forecasting ideal design parameters.

Despite the remarkable benefits of microstrip antennas, their fundamental limitation remains their inability to efficiently support multiple frequency bands within compact physical dimensions. As wireless specifications like Wi-Fi, LTE, 5G, WLAN, and satellite communications continue to expand, antennas must increasingly operate across wide and diverse frequency ranges while occupying minimal space. Fractal geometries have emerged as promising candidates for multiband performance because of their space-filling qualities and self-similarity, which enable for significant size reduction without compromising frequency behavior. However, designing and optimizing such antennas remains a challenging task due to the nonlinear relationship between geometric parameters and electromagnetic performance. Furthermore, conventional design approaches often require numerous electromagnetic simulations, which are computationally costly and time-consuming. To overcome this, artificial neural networks (ANNs) have proven effective in modeling and predicting antenna behavior, enabling rapid performance optimization.

The main limitation of conventional microstrip antennas is their inability to accommodate multiple frequency bands without structural complexity or performance trade-offs. For this reason, significant attention has been directed toward the development of compact, high-performance, multiband fractal antennas. Therefore, new techniques that integrate fractal geometry and AI-based optimization must be explored. This forms the central motivation behind the present thesis work.

1.2 Contributions and Thesis Organization

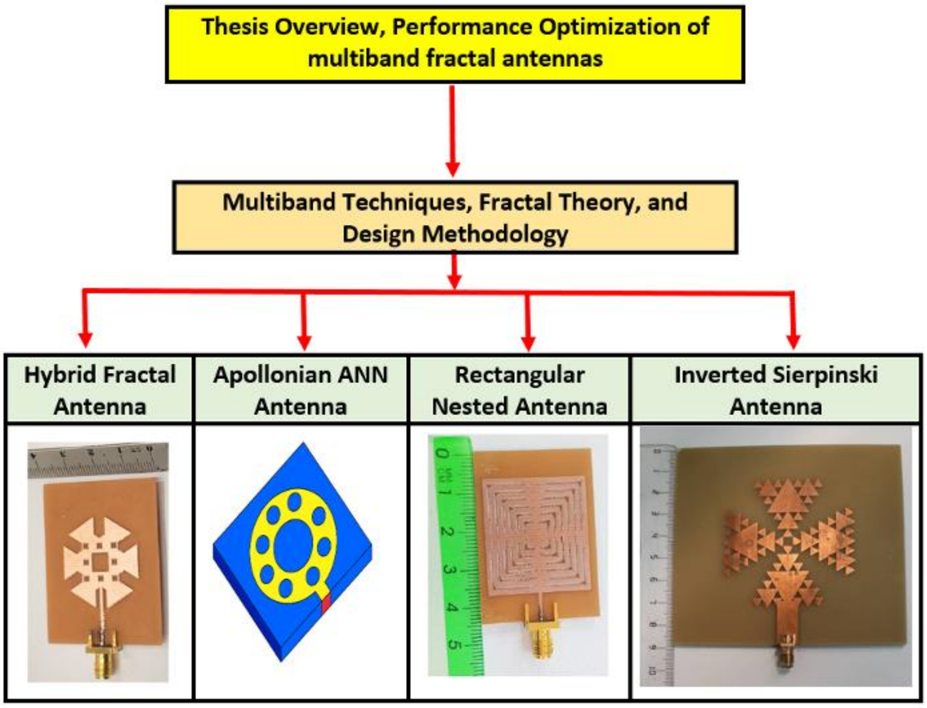

Figure 1.1: Dissertation overview

The author's contributions and the thesis outlines are arranged as follows:

Chapter Two offers an in-depth academic discussion on microstrip patch antennas, beginning with their historical development and fundamental structural principles. It examines the commonly used geometrical configurations, feeding methods, Several crucial performance factors that affect antenna performance, including return loss, VSWR, impedance, gain, efficiency, radiation pattern, bandwidth, and polarization. The chapter further introduces the concept of fractal antennas, emphasizing their unique self-similar and space-filling characteristics that enable miniaturization and multiband operation. Various fractal geometries, including Koch, Cantor, and Sierpinski structures, are reviewed to highlight their role in enhancing antenna performance. By integrating classical microstrip principles with advanced fractal design techniques, the chapter establishes the theoretical and technological foundation for the proposed research work.

Chapter Three presents a detailed overview of the design approach and development process for the proposed hybrid fractal antenna, which merges Koch snowflake and Sierpinski carpet patterns to achieve improved multiband functionality. The chapter begins by presenting the fundamental design equations and essential parameters of the microstrip patch antenna, followed by a systematic description of the successive fractal iterations that lead to the optimized final configuration. Through the progressive modification of both the patch element and the grounding layer, the antenna achieves superior impedance matching, broader bandwidth, and higher gain. A comparative evaluation with previously reported designs further underscores the advantages of the suggested antenna regarding compactness, efficiency, and multiband operation. Furthermore, the merging of Koch and Sierpinski structures provides a balanced trade-off among miniaturization and performance, as the Koch edges extend the current path while the Sierpinski slots enable multiple resonant modes. The chapter concludes by validating the design through both simulated and experimental results, These findings confirm The antenna's appropriateness for contemporary wireless applications, including 5G systems and Wi-Fi.

Chapter Four will present the design, fabrication, and ANN-based optimization of a modified Sierpinski gasket antenna. This chapter begins by discussing the motivation for employing ANN-based modeling techniques to address the shortcomings of conventional analytical and numerical methods in antenna design. A detailed review of recent ANN applications in microstrip antenna prediction and optimization is provided, followed by an in-depth description of the proposed antenna's structure, key geometric parameters, and the dataset preparation process. The architecture, activation functions, and optimization strategies of the ANN model are then systematically examined. Finally, simulation outcomes and comparative analyses are provided to confirm the correctness, efficiency, and robustness of the suggested ANN-based methodology in predicting and optimizing antenna performance.

Chapter Five will present the performance evaluation of a fractal antenna with a rectangular nest developed for use in multiband wireless technologies. This chapter begins with an overview of related research on rectangular patch and fractal antenna structures, highlighting recent advancements and innovative design strategies aimed at achieving small size, broad bandwidth and enhanced gain. The proposed antenna's design methodology is then discussed in detail, including the theoretical formulations used to determine resonant frequency, effective dielectric constant, and geometrical parameters. Successive design iterations are illustrated to demonstrate the evolution of the antenna geometry toward optimized multiband performance. The chapter further includes a comprehensive experimental and simulation-based assessment, examining important variables like gain, VSWR, return loss, and surface current distribution. Finally, a comparative analysis is provided to benchmark the proposed design against existing works, emphasizing its superior miniaturization, enhanced radiation characteristics, and stable multiband operation, verifying that it is appropriate for contemporary and developing wireless communication applications.

Chapter Six will present a comprehensive study on the automated design and optimization of an inverted Sierpinski fractal crossed bowtie antenna aimed at achieving compact size, enhanced gain, and multiband performance for current wireless communication technologies. The suggested design integrates the self-similarity and space-filling properties of the Sierpinski geometry with the broadband nature of the bowtie structure, resulting in a compact and efficient radiating element capable of operating across multiple frequency bands. Using a Python-assisted parametric modeling approach, the antenna geometry was generated iteratively to ensure structural precision and design flexibility. The antenna's performance measures, such as return loss, gain, bandwidth, and surface current distribution, were assessed using electromagnetic simulations in Ansys HFSS. A vector network analyzer (VNA) was used to experimentally test the design after it was manufactured on a FR4 substrate, showing good agreement between simulated and measured findings. Furthermore, a methodical parametric analysis was carried out to investigate the effects of feed width, ground plane length, and substrate material on antenna behavior. The results confirm that the proposed fractal bowtie configuration offers superior multiband capability and significantly improved gain compared to conventional designs. This chapter therefore establishes an efficient methodology for automated fractal antenna design and optimization, paving the way for compact high-gain antennas suitable for advanced wireless communication systems.

Chapter Seven will summarize the contributions presented in this thesis and provides suggestions for further research.

CHAPTER 2

Fractal Antenna: State of the Art

1 Introduction to Microstrip Antenna

1.1 Introduction

The foundation for printed antenna technology was laid as early as the 1950s [1]; however, practical implementation remained limited until low-loss dielectric materials became commercially available. This advancement significantly enhanced the feasibility of microstrip-based designs, prompting a surge in research and development aimed at leveraging their inherent advantages. Microstrip antennas, often referred to as patch antennas, are a type of printed antennas that consist of metallic radiating elements etched onto a dielectric substrate's surface, which is backed by a conductive ground plane [2]. These structures are fabricated using standard photolithographic techniques common in printed-circuit-board manufacturing [3]. The evolution of microstrip antennas gained significant momentum during the 1970s, facilitated by the emergence of dielectric substrates with tailored mechanical and thermal properties. As a result, microstrip antennas have become an integral component in a wide array of modern wireless and mobile communication systems [4]. Their inherent characteristics lightweight structure, low profile, mechanical robustness, and cost-effectiveness make them ideal for compact and integrated system designs [5].

Various configurations of radiating elements, substrate materials, and feeding mechanisms have been developed to meet application-specific requirements [6]. Initially confined to aerospace and defense sectors such as in missiles, aircraft, and satellite payloads, microstrip antennas have now become mainstream due to advances in fabrication techniques and materials. Today, they are extensively deployed in commercial domains as well. Key application areas include mobile and satellite communications, global positioning systems (GPS), direct-to-home (DTH) television, and even emerging biomedical applications [7]. With the continuous progression in substrate technology and antenna miniaturization, microstrip antennas are poised to replace many conventional antenna types in both civilian and defense platforms [8].

1.2 Common Shapes of a Patch Antenna

Patch antennas can be realized in a range of forms, with the most prevalent configurations being rectangular as presented in Figure 2.1, square, circular, and dipole-like forms. These geometries are widely favored because of their ease of use in theoretical modeling, simplicity of production using standard techniques, and their ability to produce desirable radiation characteristics. Figure 2.2 illustrates several of these commonly adopted patch antenna shapes as referenced in [9].

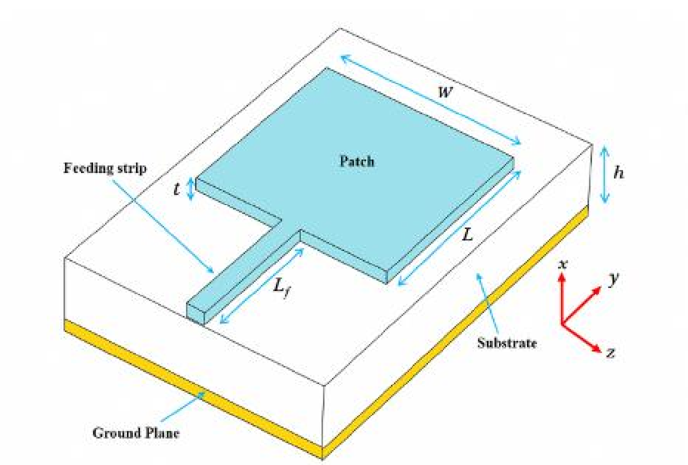

Figure 2.1: Microstrip antenna [10]

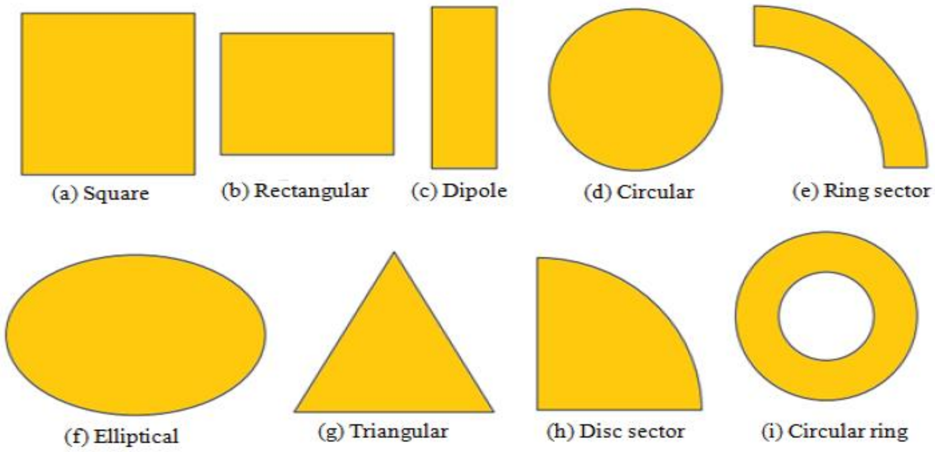

Figure 2.2: Typical microstrip patch element shapes [11]

1.3 Feeding Techniques

Various feeding techniques are employed to excite microstrip patch antennas, generally divided into two categories: contact-based and non-contact-based techniques. When using contact-based feeding, such as microstrip line and coaxial probe feed, energy is delivered directly to the radiating element. In contrast, non-contact approaches like aperture coupling and proximity coupling facilitate power transfer through electromagnetic coupling mechanisms. Additionally, coplanar waveguide (CPW) feeding represents an alternative configuration. These feeding strategies are systematically discussed in the literature [12].

1.3.1 Microstrip Line Feed

The feeding technique employed here entails connecting a conducting strip directly to the microstrip patch's edge, as illustrated in Figure 2.3. In this configuration, The feed line is directly connected to the edge of the patch, allowing the feeding structure and the radiating patch to be implemented together on a single dielectric substrate. This results in a planar and compact structure, which simplifies integration and supports low-profile antenna design [13].

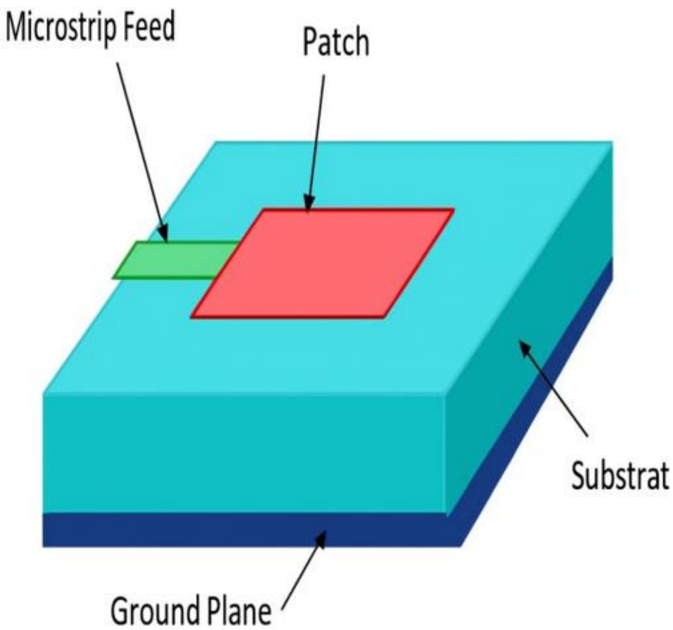

Figure 2.3: Patch element excited via a microstrip feed line[14]

1.3.2 Coaxial Probe Feed

The coaxial probe feeding technique provides a relatively limited bandwidth while producing very little undesired radiation. In this configuration, the inner conductor of the coaxial cable is connected directly to the radiating patch through the dielectric substrate [9], while the outer conductor is attached to the ground plane, as depicted in Figure 2.4. To ensure appropriate impedance matching, the feed point can be placed strategically anywhere in the patch. This technique is widely employed in microstrip antenna designs [13].

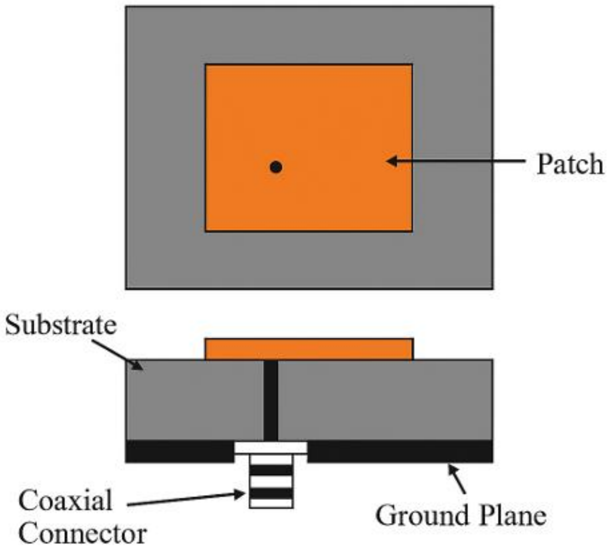

Figure 2.4: Coaxial probe excitation method[15]

1.3.3 Aperture-Coupled Feed

In the aperture-coupled feeding approach, the excitation signal is transferred to the radiating patch through a slot formed in the ground plane of the feeding structure. Unlike conventional microstrip patch antennas, this method features a distinct feed structure where the patch is electromagnetically coupled rather than directly connected, the ground plane serves as an isolating layer positioned between the patch radiator and the microstrip transmission line, with signal coupling occurring through an aperture located beneath the patch [16]. The symmetrical layout helps to suppress cross-polarization, while the degree of coupling is influenced by the feed line's geometry, size, and placement [17]. This configuration minimizes spurious radiation due to the separation of the patch and the feed by the ground plane. Typically, the bottom substrate is a thick, low-permittivity material, whereas the top substrate is thin with a high dielectric constant, as shown in Figure 2.5. However, this feeding technique is relatively complex and time-consuming to implement, requiring multiple design iterations for optimization [18].

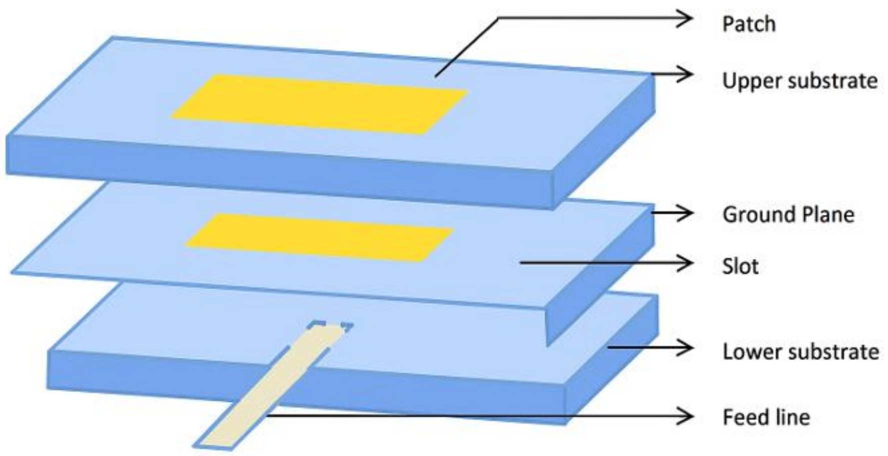

Figure 2.5: Aperture coupled feeding microstrip patch antenna [19]

1.3.4 Proximity-Coupled Feed

In the proximity-coupled feeding method, the microstrip feed line is placed between two dielectric substrate layers. Unlike edge-fed configurations, where selecting a 50-ohm feed point is challenging due to high edge impedance, this approach allows impedance matching by positioning the feed line beneath the radiating patch at a location corresponding to 50 ohms [20]. The transfer of energy from the feed to the patch occurs via electromagnetic coupling. By placing the feed line at a lower level, undesired feed radiation is significantly reduced, and the technique supports planar integration. Additionally, proximity coupling offers enhanced impedance bandwidth compared to other feeding methods [21]. However, the method involves multilayer fabrication and tends to exhibit limited polarization purity [18]. The configuration of a proximity-coupled antenna is illustrated in Figure 2.6.

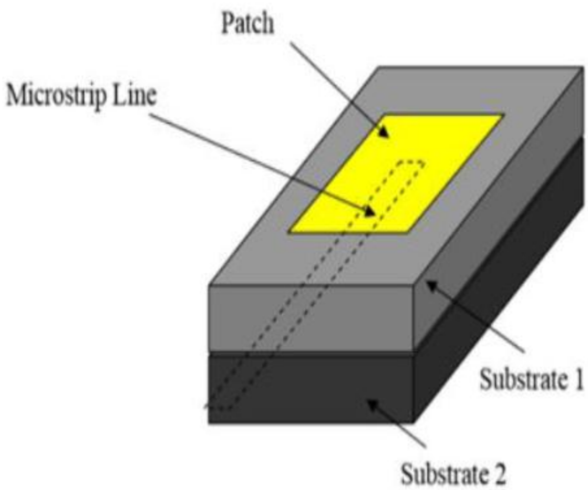

Figure 2.6: Proximity Coupled Patch antenna [22]

1.3.5 Coplanar Waveguide Feed

The coplanar waveguide (CPW) feeding technique features a signal line, ground planes, and the radiating patch, all structures are situated on the same side of the substrate, as indicated in Figure. 2.7. In this configuration, the central strip carries the signal, while the adjacent ground planes serve as the return path. The CPW feed's characteristic impedance is mainly defined by the ratio between the gap G and the width W of the signal line. This feeding method offers minimal spurious radiation and is well-suited for compact and planar antenna designs [23].

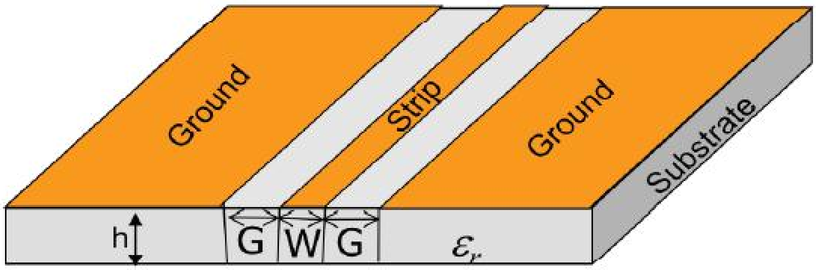

Figure 2.7: Coplanar waveguide feed [24]

1.4 Basic Parameters of Antenna

The antenna's performance is assessed using key parameters such as return loss and voltage standing wave ratio (VSWR), input impedance, directivity, gain, radiation efficiency, radiation pattern, bandwidth, and polarization characteristics. A detailed discussion of these parameters is presented below.

1.4.1 Return Loss

When the load is not properly matched, a portion of the transmitted power is not absorbed and is instead sent back toward the source, leading to power loss. This reflected power is referred to as return loss as shown in Equation (2.1), which is quantified. and expressed in decibels (dB) [9].

$$S_{11} = -20 \log (|\Gamma|) \tag{2.1}$$

1.4.2 Voltage Standing Wave Ratio (VSWR)

The Voltage Standing Wave Ratio (VSWR) quantifies the degree of impedance incompatibility between the incident and reflected waves in a transmission line as expressed in Equation (2.2). When the transmitted signal encounters a discontinuity or mismatch, part of it is reflected, resulting in the formation of standing waves. This phenomenon is expressed by the reflection coefficient (Γ), denoting the proportion of power sent back toward the source. For efficient power transfer, the magnitude of Γ should be less than 0.33, corresponding to a reflection level below $-10\,\text{dB}$ [23].

The mathematical relationship between VSWR and the reflection coefficient [9].

$$\text{VSWR} = \frac{1 + S_{11}}{1 - S_{11}} \tag{2.2}$$

The VSWR is always a positive quantity and typically falls within the range of 1 to 2 for satisfactory antenna performance. The perfect VSWR corresponds to a value of 1, signifying ideal impedance matching and zero reflected power. Therefore, achieving a value close to 1 is preferred for optimal antenna operation [25].

1.4.3 Input Impedance

The antenna's impedance is directly linked to the reflection coefficient and should match the transmission line's characteristic impedance to achieve efficient power transfer. Achieving impedance matching is critical for maximizing the delivered power to the antenna. The antenna impedance comprises both real (resistive) and imaginary (reactive) components [26] as shown in Equation (2.3).

$$Z_A = R_A + jX_A \tag{2.3}$$

Impedance mismatch leads to power loss, whereas proper matching ensures the antenna delivers the desired performance. However, proper impedance matching between the antenna and the transmission line can typically be achieved only over a specific frequency range [9].

1.4.4 Directivity

As shown in Figure 2.8, directivity quantifies the extent to which an antenna directs radiated electromagnetic energy toward a particular direction. It reflects the antenna's potential to radiate more effectively along a preferred direction compared to others.

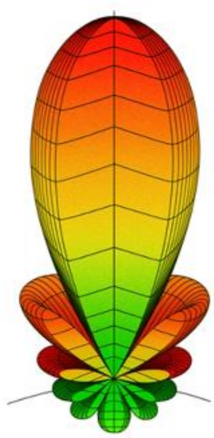

Figure 2.8: Directivity of an antenna [26]

Mathematically, directivity (denoted as D) is described as the ratio of directional radiated power to the mean radiated power over all directions [18] as indicated in Equation (2.4).

$$D(\theta, \Phi) = \frac{U(\theta, \Phi)}{U_0} \tag{2.4}$$

1.4.5 Gain

Antenna gain is a parameter that combines both efficiency and directivity, representing how effectively the antenna radiates energy in a specific direction [27]. It represents the ratio of the radiation intensity in a given direction to the radiation intensity of a perfect isotropic radiator, emitting the same total power [28] as shown in Equation (2.5). Gain is typically expressed in decibels relative to an isotropic source (dBi). Conceptually, antenna gain can be likened to the behavior of a light bulb: placing a reflector behind the bulb increases the intensity in a specific direction, analogous to increased antenna gain [9].

$$G = \eta \cdot D \tag{2.5}$$

where η represents the efficiency and D is the directivity. When the feed line and the antenna are perfectly impedance matched, the gain (G) and the realized gain (G_r) are equal. However, in the presence of impedance mismatch, the realized gain is reduced due to additional losses [29].

1.4.6 Radiation Efficiency

Antenna efficiency is determined by a combination of conduction, dielectric, and reflection efficiencies. Reflection efficiency accounts for power loss due to impedance incompatibility between the antenna and the feed line. Losses arising from conduction and dielectric properties arise from resistive losses in the conductive materials and energy dissipation within the substrate and patch surface. According to the IEEE definition, antenna efficiency is also described as the ratio of the antenna's overall power output to the power it receives. This relationship [9] can also be expressed mathematically by Equation (2.6) presented below:

$$\eta = \frac{P_{\text{rad}}}{P_{\text{in}}} \tag{2.6}$$

1.4.7 Radiation Pattern

In essence, antennas are structures or equipment made to transform electrical impulses into electromagnetic waves for transmission and back again for reception. They emit electromagnetic energy in the form of signals into free space. [9]. An antenna's radiation pattern is a visual depiction of its radiation properties as a function of spatial coordinates, as illustrated in Figure 2.9. Radiation patterns in the E-plane and H-plane are frequently used to explain the performance of linearly polarized antennas. The plane that contains both the direction of maximum radiation and the electric field vector is known as the E-plane, while the H-plane includes the magnetic field vector and the same principal direction [26]. To fully explain an antenna's radiation characteristics, three primary radiation patterns are considered: an isotropic pattern, which is an idealized reference representing a theoretical lossless antenna that radiates uniformly throughout the entire sphere and serves as a standard for comparison; a directional pattern, which exhibits higher radiation intensity in a specific direction; and an omnidirectional pattern, which radiates uniformly in the plane perpendicular to the main radiation axis, can be mathematically formulated as shown in Equation (2.7). In three-dimensional space, angular measurements of these radiation patterns are expressed in steradians, the SI unit of solid angle [18].

$$F(\theta, \phi) = \frac{E(\theta, \phi)}{E_{\max}} \tag{2.7}$$

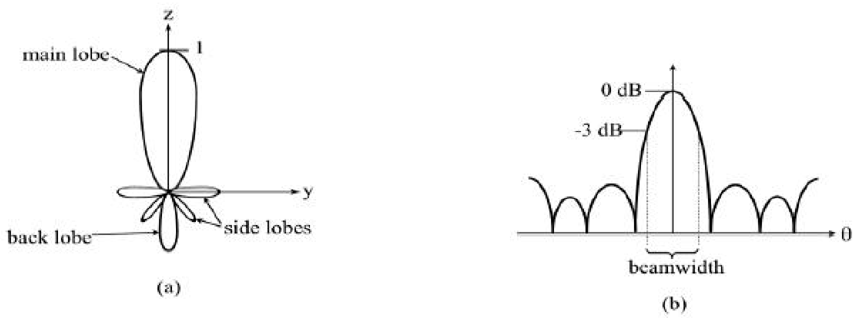

Figure 2.9: Radiation pattern representation(a) Beamwidth representation(b) [30]

The radiation pattern's highest radiation direction typically occurs along the vertical axis. The half-power beamwidth (HPBW) in the field pattern is expressed as The angular distance between the points at which the radiated field strength drops to 0.707 (or 70.7%) of its maximum value. Another type of radiation pattern is the power pattern, which represents the squared magnitude of the electric or magnetic field varying with spatial position. In this case, the half-power beamwidth is determined by identifying the angular distance among the positions from which radiation occurs falls to 0.5 (or 50%) of the maximum value [25]. This angular span between the half-power points is referred to as the half-power beamwidth and is an crucial parameter for characterizing the antenna's directional characteristics.

1.4.8 Bandwidth

Bandwidth refers to the spectrum over which an antenna operates effectively. It is described as the difference between both the higher and lower frequencies limits centered around the antenna's resonant frequency [9]. Additionally, bandwidth can be described as the band of frequencies over which the main antenna parameters such as axial ratio, efficiency, beamwidth, and side lobe levels remain within acceptable or specified limits [18]. Bandwidth is generally categorized into two types: impedance bandwidth and pattern bandwidth. The impedance bandwidth represents the frequency range in which the antenna achieves adequate impedance matching, is expressed by Equation (2.8) below [26].

$$\mathrm{BW} = \frac{f_H - f_L}{f_C} \tag{2.8}$$

In this context, f_H represents the higher cutoff frequency, f_L denotes the lower cutoff frequency, and f_C is the center frequency. The fractional bandwidth is defined as the percentage difference between the upper and lower cutoff frequencies with respect to the center frequency. Fractional bandwidth values below one percent are characteristic of narrowband devices. When an antenna exhibits a bandwidth exceeding one percent, it is classified as a wideband antenna. Antennas with bandwidths of 500 MHz or greater fall under the category of ultra-wideband (UWB) antennas [31].

1.4.9 Polarization

Polarization refers to the characteristic of an electromagnetic wave that describes the variation of the electric field's magnitude and direction over time with respect to spatial coordinates.It describes the orientation of the electric field vector as the wave travels through space. Polarization is typically categorized into three types: linear, circular, and elliptical, and it is mathematically defined by Equation (2.9). In linear polarization, the electric field changes in a straight line relative to the spatial axis. In circular polarization, the electric field rotates in a circular path with equal amplitudes along both the X and Y axes. In elliptical polarization, the electric field components differ in amplitude along the two axes, resulting in an elliptical trajectory [26].

$$\mathrm{AR} = 20\log_{10}\left(\frac{E_{\mathrm{major}}}{E_{\mathrm{minor}}}\right) \tag{2.9}$$

2 Overview of Fractal Antennas

Fractal antennas have gained recognition as a prevalent choice in wireless communication because of their unique geometric properties. These structures are particularly effective in enabling multi-band operation and in achieving significant size reduction capabilities often limited in conventional microstrip antenna designs [32]. The word "fractal" originates from the Latin term *fractus*, denoting irregular or fragmented, and refers to self-replicating patterns observable at different scales [33]. This concept originates from a branch of mathematics focused on analyzing the behavior and characteristics of such complex, self-similar shapes [34].

Fractal geometries have been employed to model complex natural structures that are challenging to describe using traditional Euclidean geometry [33]. In antenna engineering, fractal patch antennas represent an evolution of conventional patch designs by incorporating these intricate geometrical patterns. Examples of naturally occurring fractal forms are illustrated in Figure 2.10. The adoption of fractal shapes has significantly contributed to the advancement of multiband antenna design. Numerous researchers have proposed diverse fractal geometries to enable the design of antennas that can operate over wide and multiple frequency bands. Mandelbrot's foundational theory, which was inspired by naturally occurring fractals, underpins much of this work [34]. Fractal structures, characterized by their geometric complexity, are typically generated through recursive algorithms, allowing large surface areas to be embedded within limited physical spaces. Key properties including self-similarity, space-filling properties, and fractional dimensions, and limitless detail render fractal patch antennas particularly effective for achieving wideband performance, size reduction, multiband functionality, and improved radiation efficiency. Among these, iterative patterns and capability to fill space attributes are especially critical in the design of fractal-based microstrip antennas [35].

Figure 2.10: Natural fractals [36]

2.1 Fractal Properties

Fractal geometries possess several key properties that make them highly advantageous in electromagnetic applications, particularly in antenna engineering.

2.2 Self-Similarity Property

The self-similarity property of fractals is realized through iterative construction processes, where a geometric pattern is repeatedly scaled down and replicated. By applying an infinite number of iterations using simple recursive functions, multiband characteristics can be achieved. In essence, the structure consists of smaller segments that mirror the overall configuration, forming a hierarchy of reduced-scale copies embedded within the complete geometry [37]. This repetition leads to the absence of a fixed scale, as numerous miniature replicas are present throughout the design. An illustration of this kind of structure is the Fern Leaf fractal, illustrated in Figure 2.11. Scaling may occur uniformly or non-uniformly along two orthogonal directions [35]. When different scale factors are applied along each axis, the resulting geometry is classified as a self-affine fractal; if the scaling is identical in both directions, it is known as a self-similar fractal. Numerous studies have leveraged the self-similarity property of fractals to develop antennas with multiband and wideband performance [33].

Figure 2.11: Self-similar fractal- Fern Leaf [38]

2.3 Space-Filling Property

When fractal shapes are iterated extensively, they can effectively occupy a two-dimensional area even as the total curve length becomes infinitesimal small. Certain complex fractal shapes, though intricate, have been employed in antenna and array designs to enhance radiation performance. Due to their scale-independent nature, fractals allow the construction of compact antennas that maintain consistent operational frequencies regardless of physical size [39]. The multilevel space-filling characteristic of fractals has been utilized to significantly improve the antenna's gain and bandwidth over a broad frequency range, contributing to the overall miniaturization of antenna structures [40]. An example of this can be seen in the iterated Hilbert curve fractal antenna, illustrated in Figure 2.12. The space-filling characteristic plays a key role in reducing antenna size, enabling the development of more efficient, compact, and adaptable designs. Fractal-based patch antennas, because of their distinctive characteristics, are gaining recognition as a powerful solution in modern antenna engineering. The integration of fractal geometry into antenna theory has become a prominent advancement in contemporary electromagnetic design [35].

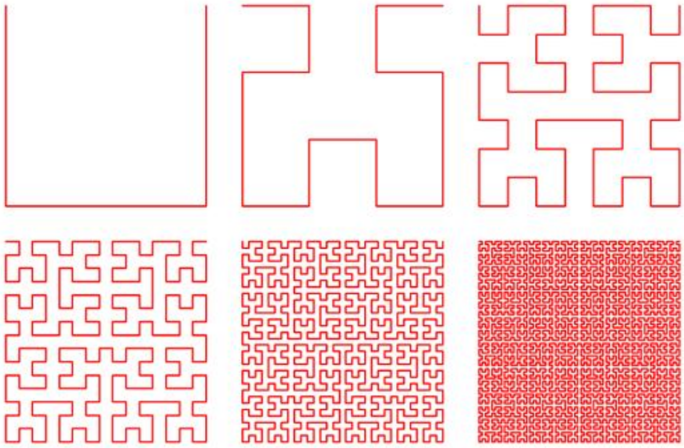

Figure 2.12: Hilbert fractal curve [41]

3 Commonly Used Fractal Geometries

The intrinsic characteristics of fractal geometries, like space-filling, self-similarity, and multiband behavior, have led to their widespread use in antenna design. Among the fractal geometries that are most frequently utilized are:

3.1 Koch Curve

The Koch curve, illustrated in Figure 2.13(a), was originally introduced by Swedish mathematician Helge von Koch, who described it as a continuous curve lacking any defined tangents [42]. In antenna engineering, this geometry has been employed to miniaturize quarter-wavelength monopole antennas, making them suitable for low-frequency applications. The Koch structure is most effectively realized using printed antenna technology, particularly microstrip patches fabricated on dielectric substrates, enabling precise control over operating frequency bands. Research has demonstrated that the Koch-shaped antenna's electrical length increases input resistance while decreasing reactance, with a corresponding downward shift in the resonant frequency [43]. These effects are attributed to the added number of corners and bends, which enhance the antenna's radiation characteristics [33]. Additionally, the Koch fractal geometry can be systematically generated using the Iterated Function System (IFS) algorithm. [44].

3.2 Cantor Set Geometry

The Cantor set, depicted in Figure 2.13(b), was introduced in 1883 by the German mathematician Georg Cantor. It comprises a sequence of intervals interspersed with systematic gaps and holds significant relevance in set theory and dynamical systems [45]. The Cantor set is created by repeatedly removing the middle third of a line segment in each iteration [46]. Due to its self-similar and sparse structure, the Cantor geometry has been investigated extensively by researchers and applied in antenna design either in its basic form or integrated with other fractal configurations to enhance various performance parameters [33].

3.3 Sierpinski Gasket Geometry

The Sierpinski gasket, or Sierpinski triangle, is named in honor of the Polish mathematician Wacław Sierpiński, who first described its characteristics [47].

This fractal can be generated using the Iterated Function System (IFS) methodology [48, 49]. It is constructed by repeatedly applying geometric transformations such as rotation, scaling, and translation to a basic triangular shape, which is then selectively removed to form the recursive pattern, as illustrated in Figure 2.13(c). The Sierpinski triangle has been extensively investigated in various antenna configurations due to its inherent repetitive pattern and multiband properties [50].

3.4 Sierpinski Carpet Geometry

The Sierpinski carpet is a widely recognized fractal structure that is generated through successive iterations using affine transformations within the Iterated Function System (IFS) framework [33]. The construction begins with a square patch serving as the initial shape. In the first iteration, the central one-ninth portion of the square obtained by scaling the patch by one-third along both the x- and y-axes is removed. This process yields the first-stage generator. Subsequent iterations involve recursively applying the same procedure to each remaining sub-square, as illustrated in Figure 2.13(d), leading to increasingly complex and space-filling geometries.

3.5 Hilbert Curve Geometry

The Hilbert curve, illustrated in Figure 2.13(e), is a recursive space-filling fractal in which each successive iteration comprises four scaled versions of the preceding stage, interconnected by additional line segments [37, 51]. This structure is recognized as a true space-filling curve due to its ability to densely occupy a two-dimensional area. It also exhibits beneficial characteristics such as self-avoidance and structural simplicity since the entire curve can be traced in a single, continuous path [37]. The Hilbert curve can be efficiently generated using Lindenmayer systems (L-systems), a common method in fractal generation [52].

3.6 Minkowski Curve Geometry

The term “Minkowski” originates from the work of German mathematician Hermann Minkowski, who introduced it in 1907 during his studies on quadratic forms and continued fractions. The Minkowski curve, depicted in Figure 2.13(f), is generated through a recursive construction process. This fractal structure has been shown to exhibit favorable resonant behavior and radiation patterns closely resembling those of a conventional straight wire dipole at corresponding frequencies. One of its key advantages lies in effective size reduction, achieving approximately 24% reduction in the first iteration and up to 44% in the second, also supporting multiband operation [50].

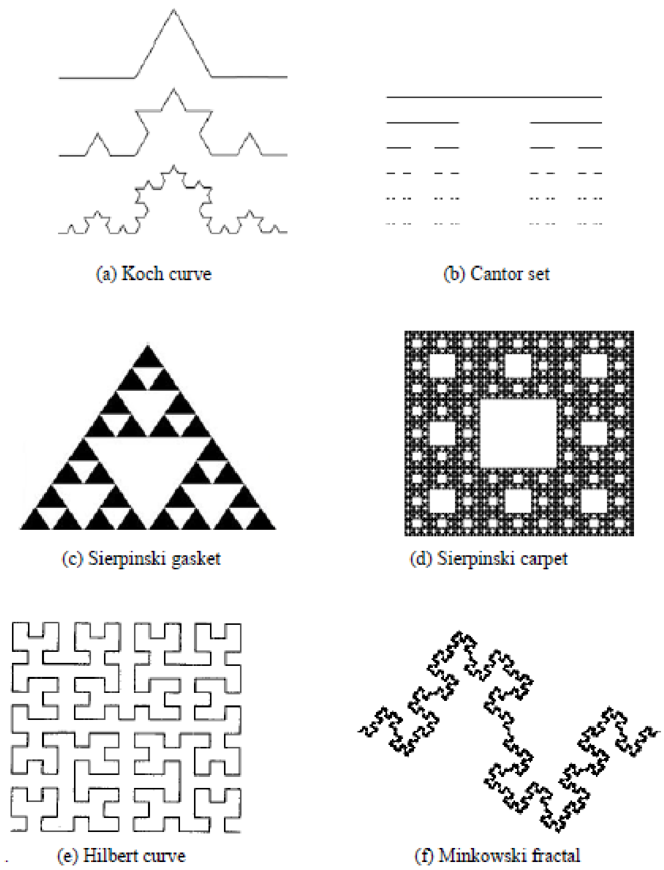

Figure 2.13: Various types of commonly used fractals geometries [53]

CHAPTER 3

Design Procedure of hybrid fractal antenna for Wi-Fi, Bluetooth and 5G applications

1 Introduction

Fractal-shaped antennas have revolutionized modern wireless engineering by combining self-repeating structures and space-filling configurations, and inherent multiple-band resonance in a compact form [54]. Configurations like the Sierpinski carpet and Koch snowflake enable multiple resonant frequencies without separate elements, improving bandwidth, gain, and radiation efficiency within a reduced footprint [55]. This fusion of mathematical elegance and practical performance addresses the needs of next-generation technologies including 5G, IoT, and millimeter-wave systems, offering cost-effective, high-performance solutions for diverse communication applications [56].

Yazid *et al.* [57] developed a compact antipodal Vivaldi antenna incorporating a Sierpinski arrowhead-shaped slot on a Rogers RO4350B substrate, operating from 2.35–3.79 GHz. The incorporation of the fractal slot enhanced the bandwidth (1.44 GHz), gain (7.35 dBi), and directivity, which makes it suitable for microwave head imaging applications while maintaining a low SAR value of 0.0013 W/kg per 10 g.

R. Kalaiyarasan *et al.* [58] developed a fractal antenna based on the Sierpinski carpet geometry with a defected ground structure (DGS) on a Rogers RO4350 substrate, resonating at 2.45 GHz. The addition of a rectangular slot in the ground plane and fractal geometry on the patch enhanced bandwidth by 23%, gain by 13%, return loss by 15%, and VSWR by 26% compared to conventional designs, making it suitable for 2.45 GHz applications involving wireless communication.

Dilaawaiz Fazal *et al.* [59] presented a multiband patch antenna design based on characteristic mode analysis (CMA) to enhance broadside radiation by superimposing lower order modes (LOMs) with higher order dominant modes (HODMs) at the same resonant frequency. By employing a single-feed technique, the antenna achieves stable, multiband operation with improved radiation performance, which makes it appropriate for 5G, and base station communication systems.

Dr. Neeraj Rao [60] proposed a modified Sierpinski fractal geometry to achieve improved miniaturization of a triangular antenna on a Rogers RO4003 ($\varepsilon_r = 4.3$). Relative to the traditional Sierpinski design, the adjusted geometry reduced the antenna size by over 50% through fourth-order fractal iteration, while maintaining satisfactory return loss (S11) and radiation characteristics, allowing it to be used for compact wireless technology.

Said Benaissa *et al.* [61] designed and experimentally validated a conformal patch antenna operating at multiple bands for ingestible bolus applications in cows, operating at 434, 868, and 1400 MHz. Integrated into a 13.5 × 3 mm^2 bolus and tested in a phantom mimicking rumen conditions, the antenna achieved gains of –36.3 to –43.6 dBi and demonstrated close correspondence between simulated and experimental results. The design supports reliable in-body biotelemetry for enhanced animal health monitoring systems.

In this chapter, an advanced antenna design incorporating Koch curves into Sierpinski fractal structures is proposed. The study focuses on enhancing the functional characteristics of a hybrid radiating element structure by exploiting the fractals' self-replicating and space-filling characteristics to accomplish compactness and multiband operation. The developed antenna exhibits high versatility, which permits its application in various current wireless communication networks, particularly 5G, Bluetooth, and related high-frequency applications. Firstly, the implementation methodology and construction process of the proposed Sierpinski–Koch fractal antenna are described. Secondly, the simulation results are presented and analyzed in detail, including the evaluation of each design version and its experimental confirmation of the fabricated prototype. Finally, the main findings of this research are summarized, and concluding remarks are provided.

2 Antenna Design

The design of the presented Koch–Sierpinski fractal antenna depicted in Figure 3.1 and Figure 3.2 was conducted using the High Frequency Structure Simulator (HFSS) version 15 through a four-stage iterative process aimed at achieving optimal multiband performance. The antenna geometry relies on the integration of two classic fractal structures: the Sierpinski carpet and Koch snowflake fractal shapes, which are known for their scale-invariant and space-filling characteristics that promote miniaturization and multiband behavior, can also be expressed mathematically by Equations (3.1), (3.2), (3.3), (3.4), (3.5), (3.6), and (3.7) presented below:.

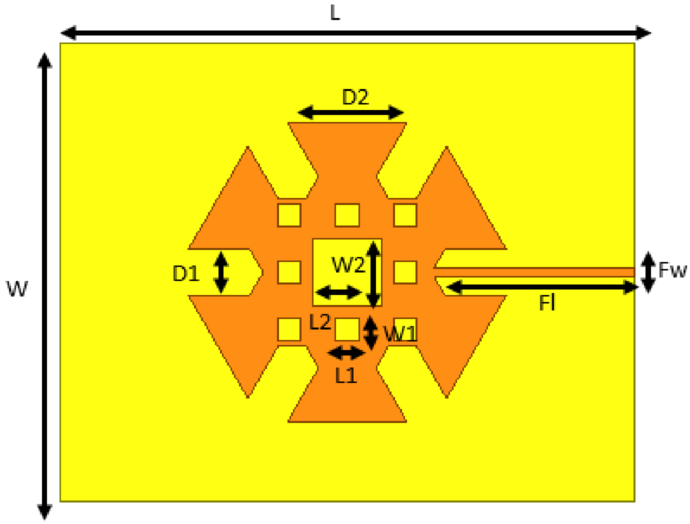

Figure 3.1: Upper view of the proposed antenna

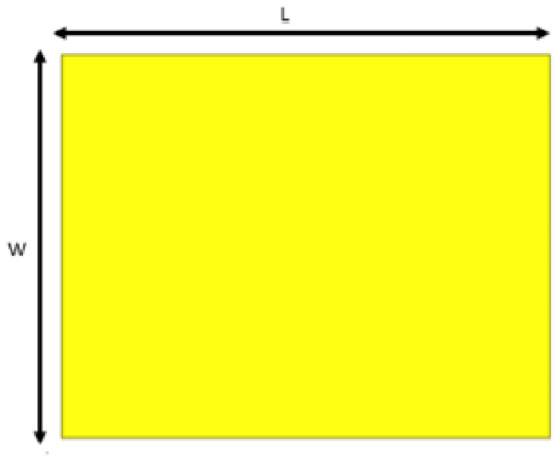

Figure 3.2: Bottom view of the presented fractal antenna

The starting side length of the equilateral triangle is specified as:

$$L_0 = a \tag{3.1}$$

where a denotes the side length of the starting triangle.

After n steps, the side length of the triangle is reduced to:

$$L_n = L_{n-1} \cdot \frac{4}{3} \tag{3.2}$$

The overall perimeter length after n iterations is given by:

$$P_n = 3 \cdot a \cdot \left(\frac{4}{3}\right)^n \tag{3.3}$$

The Koch snowflake's area following n iterations is calculated as:

$$A_n = A_0 + a^2 \frac{\sqrt{3}}{5} \cdot \left[1 - \left(\frac{4}{9}\right)^n\right] \tag{3.4}$$

where

$$A_0 = a^2 \frac{\sqrt{3}^n}{4} \tag{3.5}$$

corresponds to the area of the base equilateral triangle.

As illustrated in Figure 3.3, the initial iteration (a) begins with two overlapped equilateral triangles, forming a symmetric base structure. These are excited using a 50 Ω microstrip line to ensure efficient signal transfer and impedance matching. In the second iteration (b), a central rectangular slot is introduced, followed by eight smaller slots around it to form the Sierpinski carpet pattern. The third iteration (c) adds triangular notches on the edges of the base triangle, representing the Koch snowflake structure. The final iteration (d) integrates both fractal patterns, generating a wheel-inspired antenna suitable for multiband use.

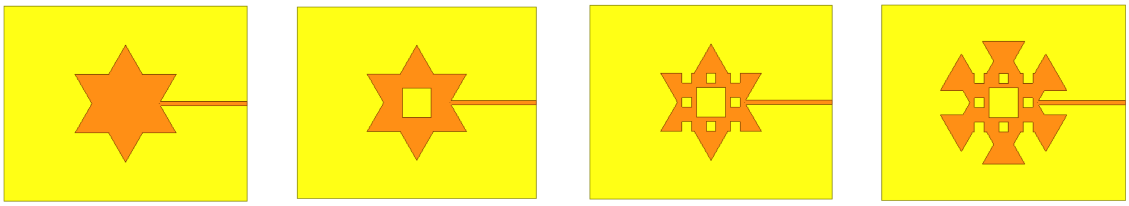

(a) (b) (c) (d)

Figure 3.3: Design process of the proposed antenna: (a) first design iteration, (b) second design iteration, (c) third design iteration, (d) fourth design iteration

The antenna is realized on an economical FR4 substrate with $\varepsilon_r = 4.7$, a thickness of 0.8 mm, and overall dimensions of 40 mm $\times$ 50 mm, as summarized in Table 3.1. A 50 Ω microstrip feed is used to achieve proper impedance matching at the port. The fabricated prototype is shown from the top and bottom views in Figures 3.4 and 3.5, respectively.

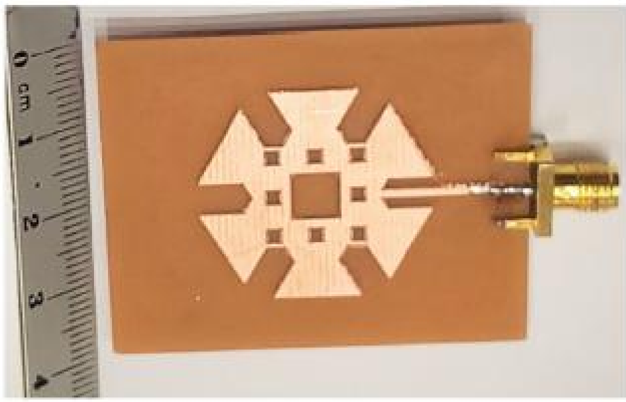

Figure 3.4: Upper view of the fabricated antenna

To validate the antenna's performance, the fabricated structure was measured with a Vector Network Analyzer (VNA), verifying the simulated characteristics and multiband behavior across the targeted frequency bands. The shape and layout of the Koch–Sierpinski fractal antenna is thus optimized for compactness, broadband operation and steady radiation behavior, making it well suited for modern wireless applications.

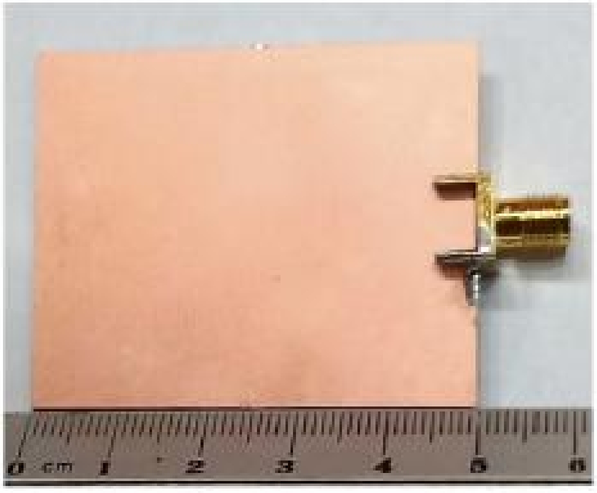

Figure 3.5: Rear view of the fabricated antenna

The Koch snowflake's fractal dimension D is determined by:

$$D = \frac{\log(4)}{\log(3)} \tag{3.6}$$

The parameter n indicates the number of fractal subdivisions performed on the original geometry:

$$n = \log_S \left(\frac{L_0}{L_n} \right) \tag{3.7}$$

where:

- L_0 refers to the length of the first rectangle.
- L_n corresponds to the rectangle length after n iterations.
- S is the reduction factor applied at each iteration.

Table 3.1: Size specifications of the antenna

Variables	Lg	Wg	Fw	Fl	D1	D2	W1	W2	L1	L2
Values (mm)	50	40	0.82	17.78	5	7.5	2	6	2	6

3 Results and Discussions

3.1 Return Loss and VSWR

Figure 3.6 illustrates the impact of several dielectric materials on the return loss effectiveness of the antenna. Among the substrates tested, the FR4 material exhibited the most favorable multiband behavior, with resonances at 2.45, 3.43, 7.69, 8.25, and 9.79 GHz.

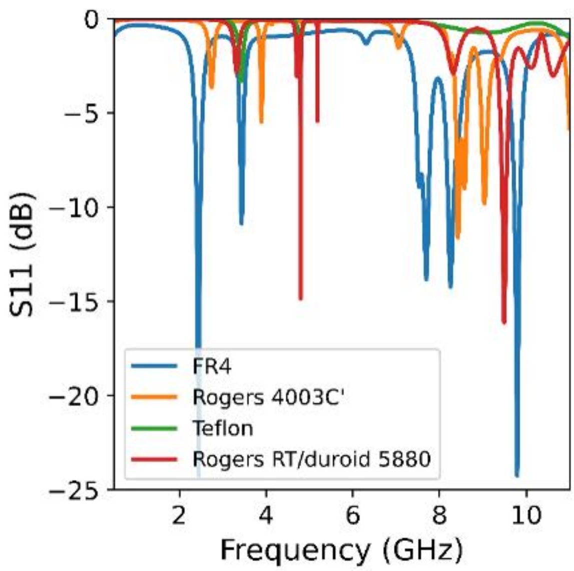

Figure 3.6: Effect of dielectric material

It achieved return loss values reaching –24.24dB, rendering it highly adaptable for use in multiband systems. In comparison, Rogers 4003C supported only two resonant bands at 8.5 GHz and 9.1 GHz, with relatively reduced return losses of –12 dB and –10 dB, respectively. Teflon and Duroid 5880 substrates also depicted dual resonances at 4.8 GHz and 9.6 GHz, reaching return losses of –15 dB and –17 dB, but with less versatility than FR4.

The reflection coefficient (Γ) can be determined using in Equation (3.8):

$$\Gamma = \frac{Z_L - Z_0}{Z_L + Z_0} \tag{3.8}$$

where:

- Z_L corresponds to the load impedance.
- Z_0 is the characteristic impedance.

It follows that the return loss can be expressed as in Equation (3.9):

$$\text{Return Loss} = -20 \log_{10} |\Gamma| \tag{3.9}$$

Figure 3.7 examines the impact of changing the microstrip feed width, ranging from 0.82 mm to 1.4 mm, on the return loss performance. Although the resonant frequencies remained relatively stable, the feed width of 0.82 mm achieved the best impedance matching, producing five resonance modes with return losses reaching approximately –24.24 dB. This indicates that a 0.82 mm feed width provides ideal feeding conditions when used in conjunction with an FR4 substrate.

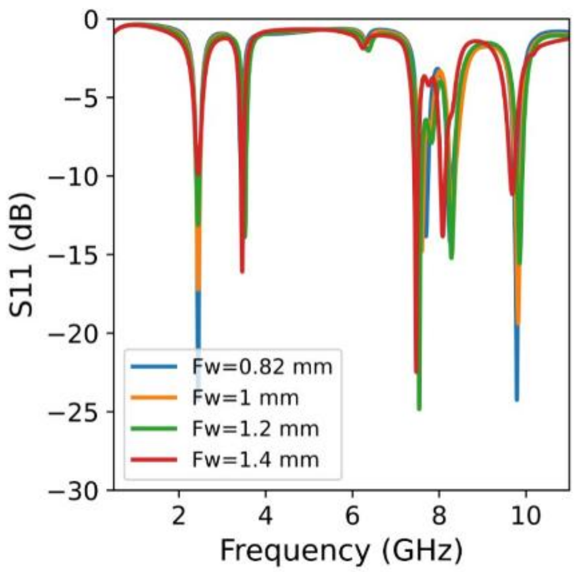

Figure 3.7: Impact of feed width

Figure 3.8 Shows the return loss behavior over the four antenna design iterations. In the first iteration, two resonant bands achieve return losses below –10dB. The second iteration shows just one strong resonant band. The third iteration also maintains a single resonance below –10 dB but lacks consistency across the bands. In the fourth and final iteration, the antenna resonates at 2.45 GHz, 3.43 GHz, 7.69 GHz, 8.25 GHz, and 9.79 GHz, with return losses of –24.24 dB, –10.86 dB, –13.83 dB, –14.21 dB, and –24.24 dB, respectively. The deepest notches at 2.45 GHz and 9.79 GHz indicate well-matched impedance. Corresponding bandwidths are 86 MHz, 202 MHz, 110 MHz, 120 MHz, and 130 MHz, with the 3.43 GHz band offering the widest bandwidth, thereby enhancing the overall antenna performance.

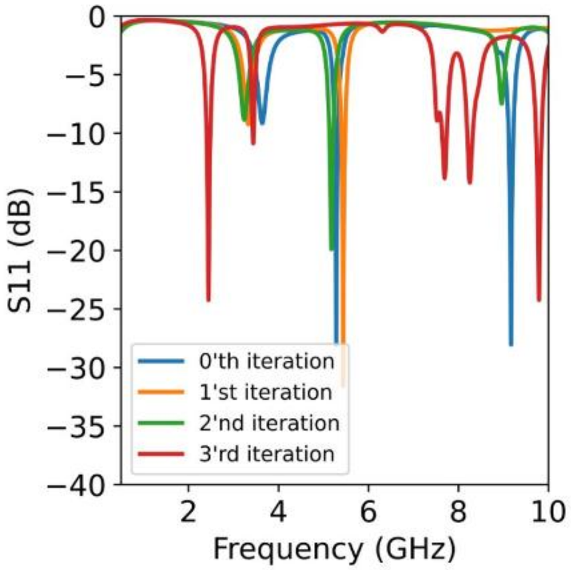

Figure 3.8: Return loss versus frequency: comparison of performance across all design iterations

Figure 3.9 contrasts the final antenna prototype's simulated and measured return loss values. The precision and dependability of the antenna design over the intended operating frequency ranges are validated by the high agreement between the simulated and measured data.

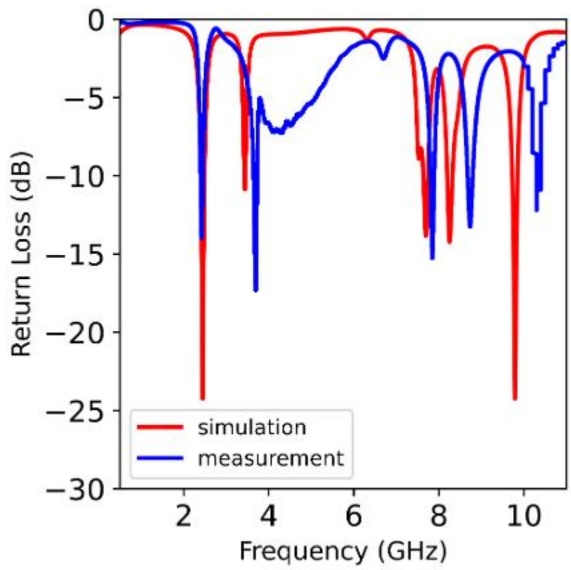

Figure 3.9: Return loss versus frequency: comparison of measured and simulated results of the antenna

Finally, Figure 3.10 illustrates the Voltage Standing Wave Ratio (VSWR) across the five resonant frequencies and it is mathematically defined by Equation (3.10).

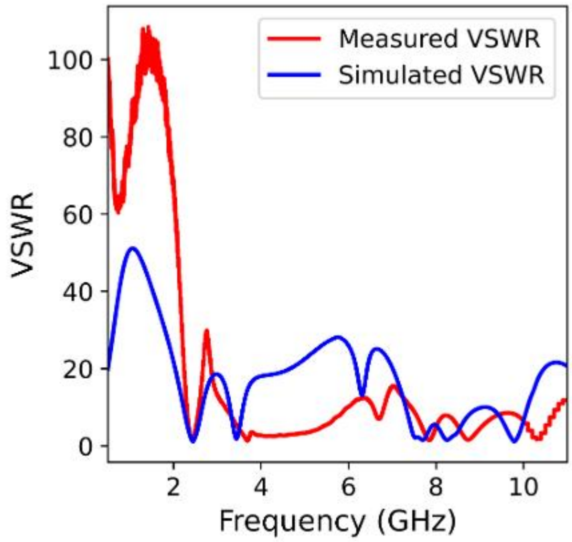

Figure 3.10: VSWR versus frequency of the proposed antenna

The VSWR values at 2.45, 3.43, 7.69, 8.25, and 9.79 GHz are 1.13, 1.81, 1.52, 1.48, and 1.13, respectively. These low VSWR values indicate excellent impedance matching and minimal signal reflection, validating the antenna's applicability for Wi-Fi, mid-band communication, and X-band radar systems

$$\text{VSWR} = \frac{1 + |\Gamma|}{1 - |\Gamma|} \tag{3.10}$$

where:

- Γ is the reflection coefficient.

3.2 Radiation Pattern and Gain

Figure 3.11 shows the radiation patterns of the antenna at its operating frequencies: 2.45 GHz, 3.43 GHz, 7.69 GHz, 8.25 GHz, and 9.79 GHz. At 2.45 GHz, the antenna features a wide beamwidth with a gain of 13.11 dBi, indicating broad azimuthal coverage suitable for general wireless applications. As frequency becomes higher to 3.43 GHz, the radiation tend to be more focused, with a narrower beamwidth and an improved gain of 18.44 dBi as shown in Figure 3.2, demonstrating stronger directivity. At higher frequencies, the gain further increases, reaching 19.48 dBi at 7.69 GHz and peaking at 29.88 dBi at 8.25 GHz, indicating highly directional radiation. At 9.79 GHz, the gain decreases to 10.22 dBi, while still maintaining sufficient directivity for targeted communication. The radiation pattern plots, depicted by red ($\phi = 90°$) and blue ($\phi = 0°$) curves, emphasize the antenna's directional behavior and energy-focusing capabilities.

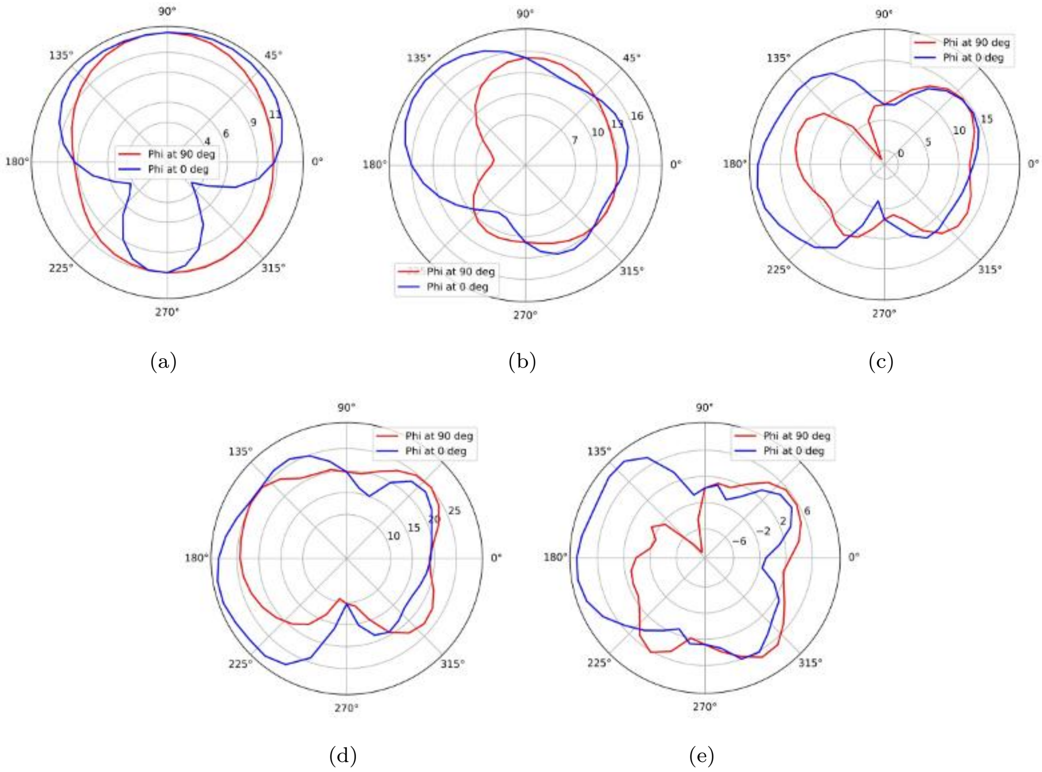

Figure 3.11: Radiation patterns for each resonant frequency: (a) 2.45 GHz, (b) 3.43 GHz, (c) 7.69 GHz, (d) 8.25 GHz, (e) 9.79 GHz

The gain $G(\theta, \phi)$ of an antenna can also be expressed mathematically by Equation (3.11) presented below:

$$G(\theta, \phi) = \eta \cdot D(\theta, \phi) \tag{3.11}$$

where:

- $G(\theta, \phi)$ represents the antenna gain along the direction (θ, ϕ).
- η represents the antenna's efficiency
- $D(\theta, \phi)$ denotes the directivity of the antenna in the specified direction (θ, ϕ).

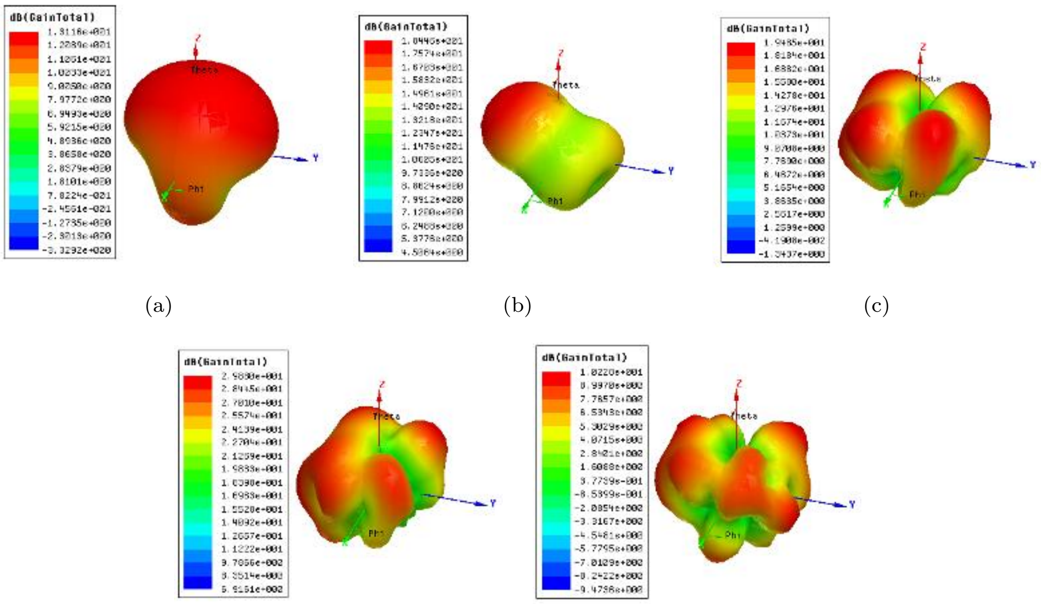

(a) (b) (c)

(d) (e)

Figure 3.12: G
ain performance at each resonant frequency: (a) 2.45 GHz, (b) 3.43 GHz, (c) 7.69 GHz, (d) 8.25 GHz, (e) 9.79 GHz

3.3 Surface Current Distribution

Figure 3.13 shows the surface current distribution of the proposed antenna at its resonant frequencies: 2.45 GHz, 3.43 GHz, 7.69 GHz, 8.25 GHz, and 9.79 GHz. At 2.45 GHz, the current is predominantly focused along the feed line and the central region of the radiating patch, indicating effective power delivery and strong coupling between the source and the radiating structure. As the frequency rises, the current progressively shifts toward the edges and corners of the antenna. This redistribution enhances radiation efficiency and contributes to improved directivity at higher frequency bands. The observed current flow behavior confirms the efficiency of the iterative design process approach in enabling multiband operation with enhanced electromagnetic performance across the selected frequency spectrum.

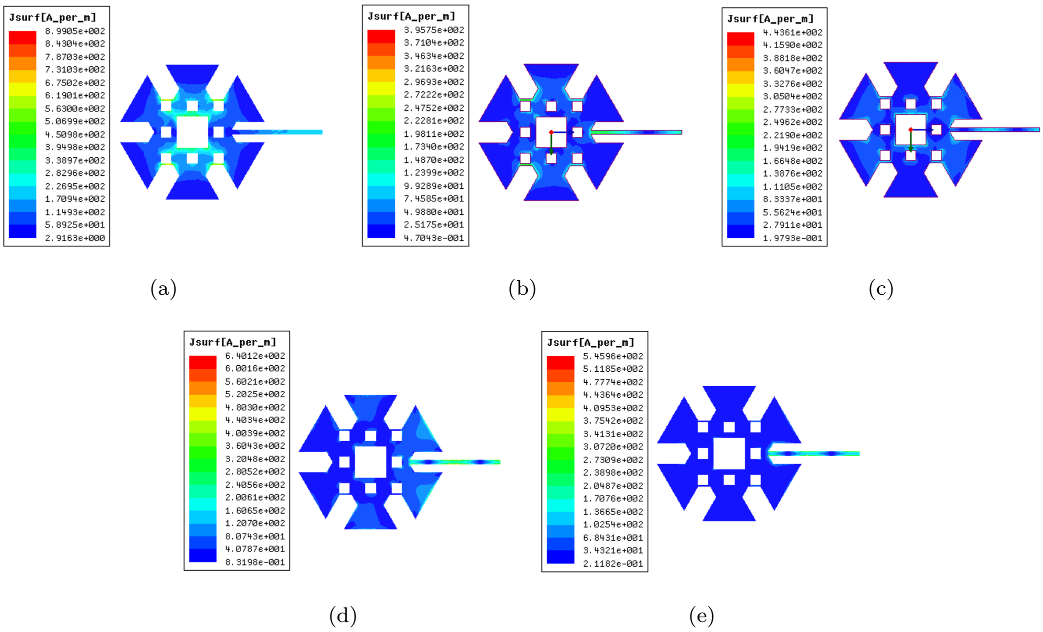

Figure 3.13: Surface current patterns at the resonant frequencies: (a) 2.45 GHz, (b) 3.43 GHz, (c) 7.69 GHz, (d) 8.25 GHz, (e) 9.79 GHz

Figure 3.14 presents the fabricated prototype of the antenna connected to a Vector Network Analyzer (VNA) for experimental testing. This setup demonstrates the realization of the antenna and serves to validate its simulated performance.

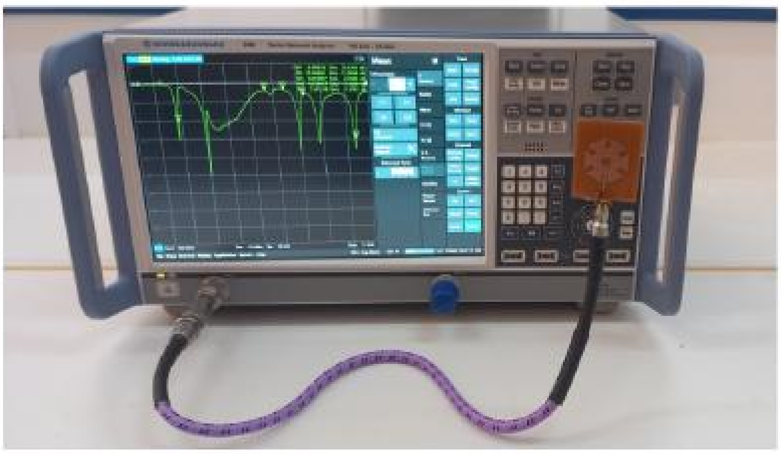

Figure 3.14: Fabricated proposed antenna with VNA

The measurement configuration ensures accurate assessment of key parameters such as return loss and impedance matching, confirming the performance of the design under real-world conditions.

Table 3.2 offers a comparative analysis overview of the suggested antenna versus various prior published designs, highlighting its superior performance across multiple parameters. With compact size of 40 × 50 mm^2, the proposed antenna is the smallest among all compared designs, yet it supports five distinct operating frequencies (2.45, 3.43, 7.69, 8.25, and 9.79 GHz), offering the highest multiband capability. In contrast, other antennas [57, 61] operate over only one to three bands with significantly larger form factors. Notably, the proposed antenna demonstrates a maximum gain of 29.88 dBi, which substantially surpasses the gains reported in related works, such as 7.35 dBi in [57] and 8.99 dBi in [59]. Although the antenna presented in [61] supports multiple bands, its gain performance is extremely poor (as low as –38.5 dBi), indicating low radiation efficiency. Overall, the proposed antenna successfully combines high gain, broad multiband support, and compact size,making it an excellent option for radar and sophisticated wireless applications.

Table 3.2: Comparison with other published work

Ref	**Size (mm^2)**	**No. Bands**	**Gain (dBi)**	**Resonant Frequencies (GHz)**
[57]	65×65	2	7.35	2.35, 3.79
[58]	52×71	1	4.4	2.45
[59]	80×80	3	8.99	3.27, 4.88, 5.33
[60]	53×53	2	6.82	4.63, 6.39
[61]	87×100	3	-38.5	0.43, 0.86, 1.4
Prop. [62]	40×50	5	29.88	2.45, 3.43, 7.69, 8.25, 9.79

4 Summary

In summary, the proposed study presents a compact and high-performance multiband antenna based on a hybrid fractal configuration that combines the Sierpinski carpet geometry and Koch snowflake structure. Designed to operate at five operating frequencies 2.45, 3.43, 7.69, 8.25, and 9.79 GHz the antenna exhibits excellent suitability for several applications such as Wi-Fi,5G, Bluetooth, satellite communication, and radar systems. It achieves return loss values as low as –24.24 dB, VSWR below 1.81, and bandwidths varying from 86 MHz to 202 MHz, ensuring strong impedance matching and stable multiband operation. With a maximum gain of 29.88 dBi and a compact footprint of 40×50 mm^2, the proposed antenna significantly outperforms several existing designs in both radiation efficiency and frequency coverage, establishing it as a robust candidate for wireless and sensing applications.

CHAPTER 4

Design and Optimisation of Modified Apollonian Gasket Using Artificial Neural Networks

1 Introduction

Artificial Neural Networks (ANNs) have proven to be an effective approach for the analysis and design of microstrip antennas, offering a promising alternative to conventional analytical and numerical methods. While traditional models such as transmission line theory and cavity models simplify radiation behaviour, often at the expense of accuracy, full-wave electromagnetic simulations demand significant computational resources. ANN-based approaches bridge this gap by providing fast, accurate predictions of antenna parameters. Recent scholarly studies have established that the effectiveness of ANN models in optimizing key performance metrics like return loss, resonant frequency, gain, and impedance matching, enabling efficient antenna design for complex, multi-band wireless applications.

Haizhuo He *et al.*[63] proposed an ANN-based model to predict the S-parameters, gain, and directivity of antenna centered at 10.2 GHz with a 1 GHz bandwidth. By fitting EM-CAD–generated response data to rational functions characterized by orders, residues, and poles, their approach replaces traditional performance metrics with these function parameters, and validation tests confirmed the model's accuracy and efficiency.

Jing Rui Wang *et al.*[64] developed a triple-band microstrip patch antenna optimized using ANN for WLAN applications. The antenna, designed with two metal patches on an FR4 substrate, operates at 1.52 GHz, 2.46 GHz, and 2.79

GHz. A dataset of 162 samples generated via HFSS and based on four geometric and material parameters was employed to train and verify the ANN model for bandwidth optimization. The results showed minimal average percentage error and reliable gain performance, confirming the the antenna's capability for multi-band operation WLAN systems.

Francismari Noronha dos Santos *et al.*[65] introduced an ANN-based approach for analyzing and designing various shapes of microstrip antennas by modeling the relationship between key parameters such as frequency, physical dimensions, and dielectric constant. Unlike traditional analytical models like the transmission line or cavity model which simplify radiation mechanisms and can introduce inaccuracies, the proposed ANN method offers a more efficient alternative to computationally intensive numerical techniques, providing accurate predictions with reduced complexity and faster processing.

Aarti Gehani *et al.*[66] analyzed a circularly polarized elliptical antenna using ANN model. The input variables included the semi-major axis radius, feed location, and substrate height, while the outputs were the resonant frequency and return loss. The ANN predictions closely matched simulation results, demonstrating the model's effectiveness in accurately estimating antenna performance with reduced computational effort.

Hemraj Kumawat and Poonam Agarwal[67] proposed an ANN-based model to predict the physical variables of an inset-fed antenna. With input variables utilizing inputs like operating frequency, substrate height, and dielectric constant, the model determines the patch width, patch length, inset depth, feed line width, and notch gap. Utilizing a feed-forward back-propagation architecture optimized via the Adam optimizer, the model was refined by tuning batch size, hidden layers, and epochs. The final model achieved strong predictive performance, with an MSE of 0.2249, RMSE of 0.4742, and MAE of 0.2075 on the test dataset.

Ivan Vilovic and Niksa Burum[68] developed neural network models to assist in the design and feed position estimation of circular antennas. A multilayer perceptron (MLP) was employed to predict the physical and effective radius along with the antenna's directivity, while a radial basis function (RBF) neural network was employed to estimate the optimal feed position. The proposed models demonstrated strong agreement with experimental results, confirming their accuracy and utility in efficient circular antenna design.

Ijaz Khan *et al.*[69] designed an annular ring antenna using an ANN to accurately predict resonant frequencies across various wireless communication bands, including GSM, LTE, WLAN, and WiMAX. A multilayer perceptron (MLP) trained via backpropagation was employed, using a dataset of 70 ARMA designs for training and 10 for testing. Among the different learning algorithms evaluated, the Levenberg–Marquardt (LM) algorithm yielded the highest prediction accuracy, effectively modeling the relationship between antenna dimensions and their corresponding resonant frequencies.

Bishal Dey Sarkar *et al.*[70] proposed an ANN-based model to precisely estimate the resonant frequency of a antenna by inputting key geometric parameters such as length, width, height, and dielectric constant. The model's outputs were compared with traditional theoretical design equations, demonstrating excellent agreement. Focused on the Ku-band (12–18 GHz), relevant for satellite applications, the model utilized neural network training algorithms to minimize prediction error and ensure high accuracy in frequency estimation across the specified band.

In this chapter, a distinctive antenna design based on a modified Apollonian gasket fractal structure is proposed. The performance of the antenna is optimized using artificial neural networks, providing a deeper understanding and comprehensive analysis of its electromagnetic behavior and performance enhancement. This approach offers valuable insights into the relationship between the antenna's physical structure and operational performance. Firstly, the geometric configuration and design concept of the modified Apollonian gasket fractal antenna are presented, emphasizing its unique structural features and their impact on key performance parameters. Secondly, the architecture and implementation of the artificial neural network model employed for optimization are described in detail. Finally, the validation results and analytical discussions are provided, followed by concluding remarks summarizing the principal contributions and the outcomes of this research.

2 Antenna Design

The introduced antenna configuration is based on a modified version of the classical Apollonian gasket geometry, known for its recursive self-similar and space-occupying features, which are advantageous for achieving multiband operation. As illustrated in Figure 4.1, The antenna is implemented on a low-cost FR4 glass epoxy substrate, featuring a thickness of 1.6mm and a relative dielectric constant (ε_r) of 4.4. Its small footprint of $30 \times 30, \text{mm}^2$ enables seamless integration into modern compact wireless systems. The patch area can be written in analytical form as in Equation (4.1):

$$\text{Area} = \pi r^2 - \pi r_{\text{rad}}^2 - \pi r_{\text{radi}}^2 \tag{4.1}$$

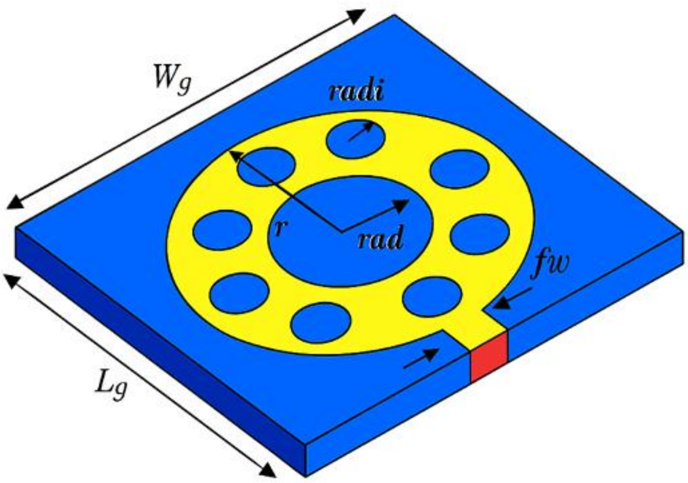

Figure 4.1: Proposed antenna structure

The design incorporates several key geometric parameters that critically influence the antenna's performance. The feed width parameter, denoted as fw, plays a significant role in ensuring proper impedance matching to enhance overall signal transmission along the microstrip line. Parameters *rad* and *radi* represent the radius and position of the central and surrounding circular elements that form the fractal layout. These variables directly impact the radiation pattern, gain, and directivity of the antenna.

Another essential variable, r, governs the size of the circular patch and is linked to the antenna's resonant frequencies and bandwidth characteristics. To systematically evaluate the influence of each parameter on the operational performance of the antenna across multiple frequency bands, a comprehensive dataset was generated, with the variable ranges and frequency inputs summarized in Table 4.1.

Table 4.1: the set of parameter values

Parameter	**Min value**	**Max value**	**Count**
`freq`	7.4 GHz	9.8 GHz	100
`fw`	1 mm	3 mm	8
`r`	12 mm	12 mm	N/A
`rad`	3 mm	6 mm	5
`radi`	0.5 mm	2 mm	5
`Wg`	30 mm	30 mm	N/A
`Lg`	30 mm	30 mm	N/A

The dataset provides the foundation for the development of an ANN model, aimed at optimizing antenna performance through intelligent parameter tuning, as outlined in the flowchart in Figure 4.2.

3 Artificial Neural Networks Model Architecture

3.1 Data Collections

To develop the predictive model, a comprehensive dataset comprising 20,000 samples was constructed, spanning the frequency range from 7.4 GHz to 9.8 GHz. The dataset included variations in key geometric parameters such as feed line widths and the dimensions of the central circular patch along with its sub-circles, corresponding to different segments of the frequency spectrum.

These data points were generated from 200 distinct simulations conducted using High Frequency Structure Simulator (HFSS), with both the real and imaginary components of the S_{11} parameter (return loss, expressed in decibels) extracted and compiled in an Excel spreadsheet. This curated dataset served as the foundation for training a machine learning model aimed at optimizing the antenna's design parameters.

Prior to training, the data underwent rigorous preprocessing to maintain its quality, consistency, and fitness for computational analysis.

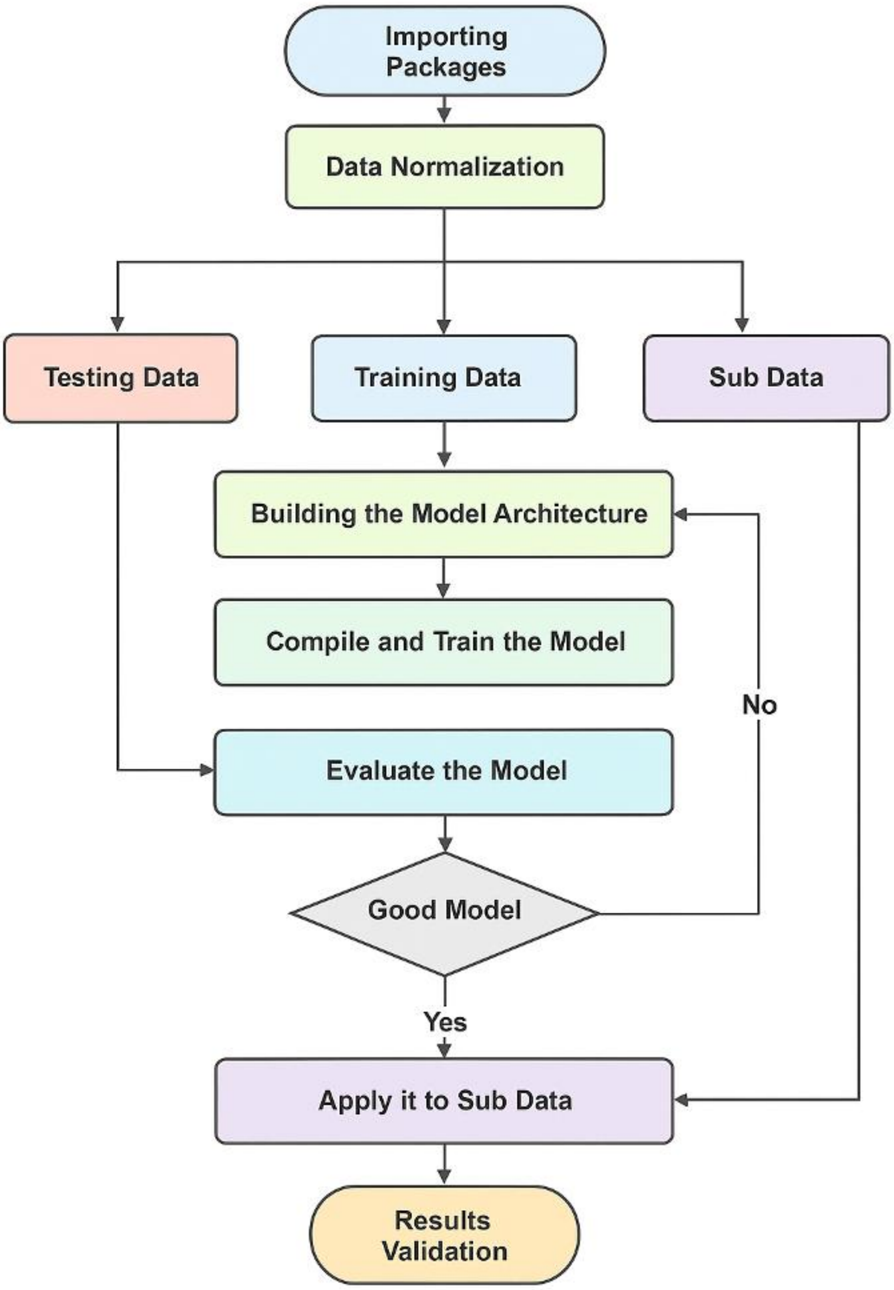

Figure 4.2: Flowchart of the proposed ANN model

3.2 Artificial Neural Networks Model Structure

To achieve reliable and accurate predictive performance, the model architecture was refined through iterative experimentation, involving systematic adjustments to the number of hidden layers and neurons. Prior to finalizing the optimal network configuration, numerous training trials were conducted to evaluate the effectiveness of various structural arrangements, the architecture of the ANN model is illustrated in Figure 4.3.

The resulting model comprises eight layers, with the Rectified Linear Unit (ReLU) and Sigmoid functions selected as activation mechanisms to introduce non-linearity and enhance learning capability across the network.

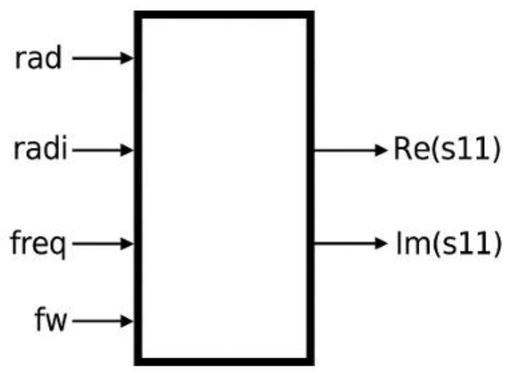

Figure 4.3: Proposed ANN model network

3.3 Activation Function

Choosing a suitable activation function plays a pivotal role in examining the behavior and effectiveness of a neural network, as it governs the activation of neurons and facilitates non-linear transformations within the model.

Among the most widely adopted functions, the Rectified Linear Unit (ReLU) has attracted significant attention in recent years due to its computational efficiency and rapid convergence characteristics. In the proposed model, ReLU has been employed in several hidden layers to enhance learning speed and model stability, while the Sigmoid function is utilized in others to support smooth gradient propagation, they are mathematically defined by Equations (4.2), (4.3), and (4.4).

$$\text{ReLU}(x) = \max(0, x) \tag{4.2}$$

$$\text{Sigmoid}(x) = \frac{1}{1 + e^{-x}} \tag{4.3}$$

$$f(x) = \begin{cases} 0, & x < 0 \\ x, & x \geq 0 \end{cases} \tag{4.4}$$

For the output layer, a linear activation function has been applied, as it is particularly well-suited for regression-based tasks. Modern deep learning architectures frequently incorporate a combination of ReLU and Sigmoid activations, and careful assignment of these functions across different layers is essential to optimize model convergence and overall predictive performance.

3.4 Optimize Function

In contemporary deep learning architectures, the choice of an optimization algorithm is critical, as it directly influences both the efficiency of the process of training and the network's performance outcomes. Given the diverse nature of learning tasks, selecting an appropriate optimizer is essential to ensure convergence stability and effective parameter tuning.

In the present study, the Adam optimizer has been employed because of its adaptive learning rate and efficient computation. These attributes make it particularly suitable for training complex neural networks, such as those used in antenna design, where accurate modeling of nonlinear relationships is required for optimal performance.

3.5 Data Processing

The dataset comprises a wide range of input and output values representing key antenna design parameters and their corresponding performance metrics. To effectively train and evaluate the neural network, the dataset was partitioned using a standard split in which 80% of the data was employed for training and 20% for evaluation

Prior to model development, Min-Max scaling may be employed to model as given in Equation (4.5), a widely recognized normalization technique, was applied to rescale the data within a defined range. This preprocessing step ensures uniformity across the dataset, facilitating improved convergence during training and enhancing the overall predictive accuracy of the model.

$$x' = \frac{x - x_{\min}}{x_{\max} - x_{\min}} \tag{4.5}$$

3.6 Network Training

The proposed neural network model incorporates four input features, each representing critical design parameters of the antenna. To analyze the model's predictive accuracy, the Mean Squared Error (MSE) was used as the main criterion for performance assessment, owing to its sensitivity to large deviations and suitability for regression tasks.

The network architecture employs a combination of Rectified Linear Unit (ReLU) and Sigmoid activation functions across its hidden layers to introduce non-linearity and facilitate effective learning. During training, the dataset is processed in various batch sizes, and the number of training epochs is iteratively adjusted to ensure optimal convergence.

Furthermore, the model is subjected to comprehensive fine-tuning, wherein hyperparameters such as the learning rate and model regularization strategies are carefully optimized to improve generalization capability and minimize overfitting, thus boosting the model's robustness and reliability.

1. Objective Function for ANN Optimization: The ANN is trained to minimize the return loss over a range of frequencies and design parameters. The objective function can be illustrated as written below Equation (4.6):

$$\text{Minimize } f(x) = \sum_{i=1}^{n} |RL(f_i, x)| \tag{4.6}$$

where $RL(f_i, x)$ represents the return loss at frequency f_i given the design parameter vector x. The objective is to determine the parameter set x that minimizes the return loss across all target frequencies.

2. Training Error (Loss Function) in ANN: During the training of the ANN, a the loss function quantifies the discrepancy between the predicted return loss values and the actual values. A common loss function for regression tasks in ANN is the MSE:

MSE is presented by Equation (4.7) :

$$\text{MSE} = \frac{1}{N}\sum_{i=1}^{N}(y_i - \hat{y}_i)^2 \tag{4.7}$$

where y_i are the true return loss values and $\hat{y}_i$ are the predicted values by the ANN.

The Gradient Descent Update Rule can be described using Equation (4.8):

$$\theta_{\text{new}} = \theta_{\text{old}} - \eta \cdot \nabla_\theta \text{MSE} \tag{4.8}$$

where θ represents the ANN parameters (weights and biases), η is the learning rate, and ∇_θMSE is the gradient of the loss function with respect to θ.

3.7 Network Tuning

To further improve the performance of the proposed ANN model, a systematic tuning process was carried out. This optimization involved iterative adjustments to both the number of training epochs and the structure of the hidden layers, allowing a thorough evaluation of the network's responsiveness to architectural changes.

The activation functions employed in the network include Rectified Linear Unit (ReLU) and Sigmoid, both of which contribute to enhancing the model's learning capacity by introducing non-linear transformations critical for capturing complex patterns within the dataset.

4 Results and Discussion

Figure 4.4 presents a detailed illustration of the model's training and validation progression, clearly demonstrating the convergence of loss values toward optimal levels a strong indication of effective learning and generalization. The remarkably low test loss of 0.012% reflects the model's high-performance ability to generalize beyond the training dataset.

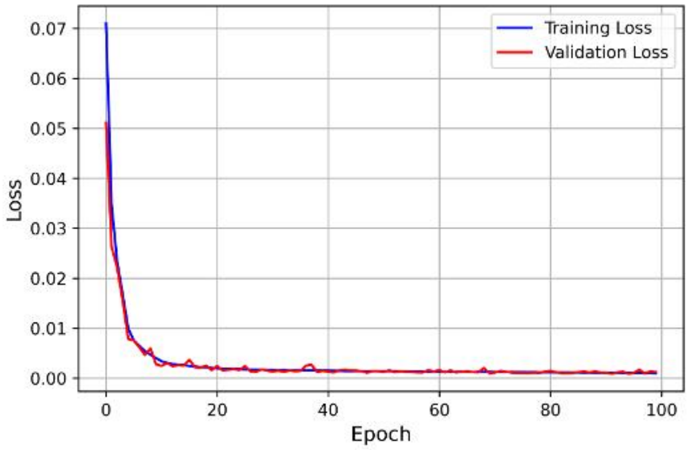

Figure 4.4: Training and validation loss over epochs

The training loss, depicted by the blue curve, highlights the model's successful calibration to the inherent complexity of the training data. This visualization not only affirms the soundness of the training methodology but also opens avenues for prospective advancements in the model's performance across broader datasets.

Complementing this, Figure 4.5 compares the real part of the ANN-predicted values with the actual values obtained from HFSS simulations. The diagonal alignment of the majority of the data points rendered in blue demonstrates a high degree of consistency between predicted and actual values.

Only a limited number of outliers deviate from this alignment, further attesting to the model's accuracy and its effectiveness in revealing the essential electromagnetic behavior with high precision.

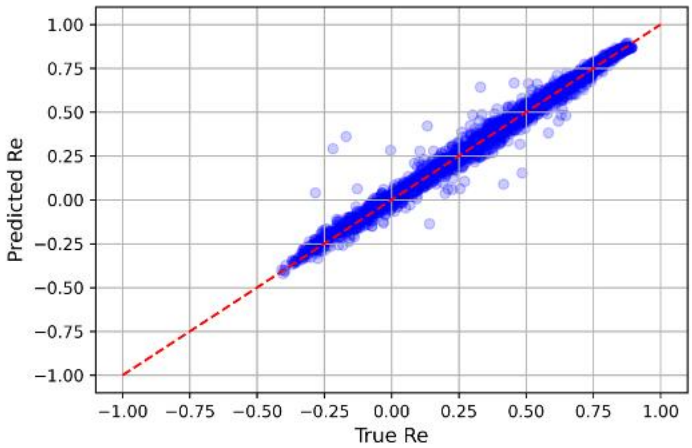

Figure 4.5: Comparison of ANN-predicted Re and HFSS-simulated Re

Figure 4.6 illustrates the comparison between the imaginary component of the actual data and that of the predicted values generated by the optimized ANN model. The results are plotted along a diagonal axis in green, revealing a high degree of alignment between the two datasets.

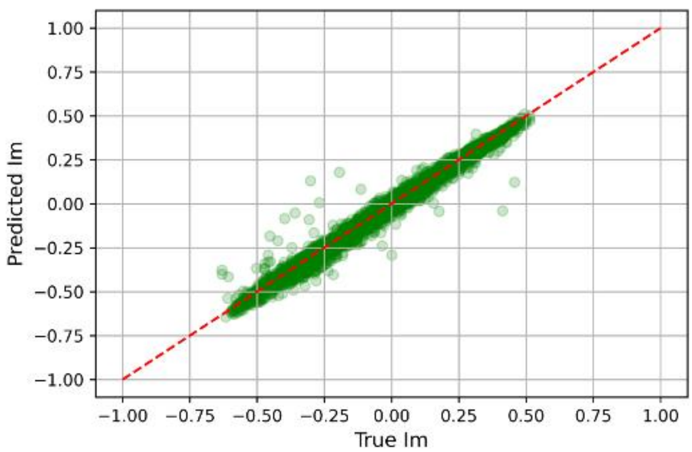

Figure 4.6: Evaluation of ANN Im predictions against HFSS-simulated Im

The close correspondence, with only a minimal number of deviations, reflects the the model's competence to precisely learn and replicate the complex behavior inherent in the imaginary part of the electromagnetic response. This strong alignment confirms the network's ability to generalize effectively and reinforces its reliability in modeling the subtle variations found within the data.

The consistency observed across the bulk of the samples further highlights the model's robustness and its proficiency in capturing the underlying physical phenomena with precision.

Figure 4.7 presents a comparative analysis of both the real and imaginary components of the training data versus those predicted by the optimized ANN model, with the HFSS data shown in green and the ANN output in blue.

The close alignment between corresponding samples in both datasets reflects the model's exceptional accuracy and effective training, demonstrating its capability to learn and replicate complex electromagnetic responses. This consistency underscores the ANN's reliability in modeling both the real and imaginary parts of the return loss parameter (S_{11}).

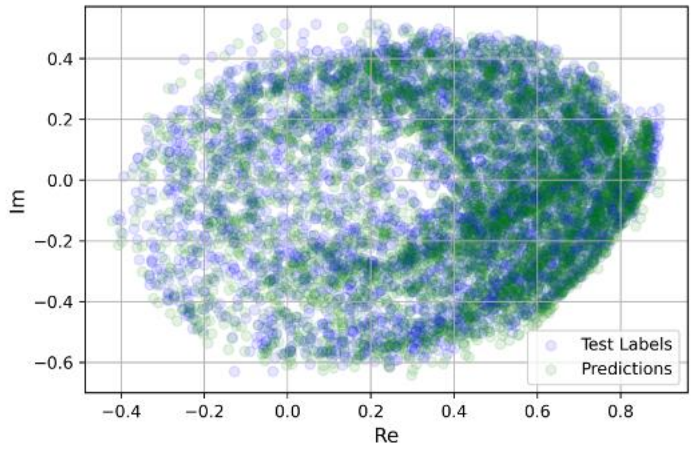

Figure 4.7: Comparison of ANN-predicted Re–Im and HFSS-simulated Re–Im

Furthermore, Figure 4.8 plots the model-estimated and actual values of S_{11} across the frequency spectrum, illustrating the model's precision in capturing frequency-dependent variations.

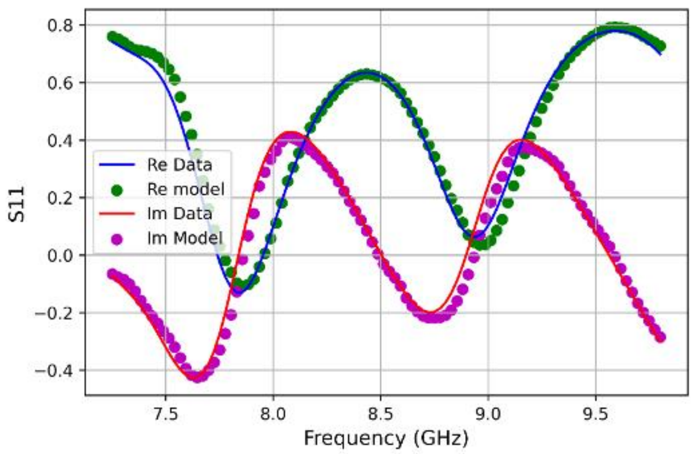

Figure 4.8: Comparison of predicted and true values from HFSS and ANN models across frequency

Moving to Figure 4.9, the magnitude of the S_{11} parameter representing the strength of the reflected signal is plotted for both the ANN model and HFSS simulations. In RF engineering, the magnitude of S_{11} ranges between 0 and 1, where a value near 0 signifies ideal transmission with minimal reflection, while a value near 1 indicates complete reflection.

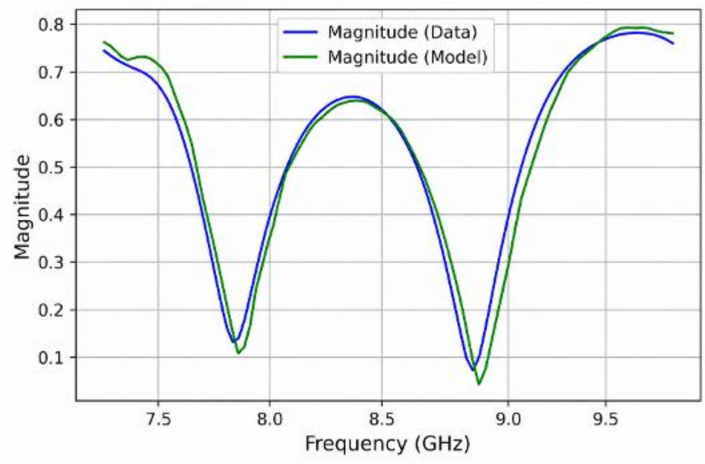

Figure 4.9: ANN model versus HFSS simulation magnitudes as a function of frequency

Practically, this is often expressed in decibels (dB) to assess antenna performance. The green curve representing the ANN prediction maintains a magnitude below 0.1, signaling excellent impedance matching and confirming the model's success in optimizing antenna characteristics for minimal signal reflection.

Figure 4.10 illustrates a comparative plot of the phase response of the antenna in terms of frequency, with the blue curve representing the original HFSS training data and the green curve denoting the phase predicted by the enhanced ANN model. This graphical comparison provides valuable insight into the model's fidelity, revealing a strong correlation between the simulated and predicted phase characteristics across the operating frequency range.

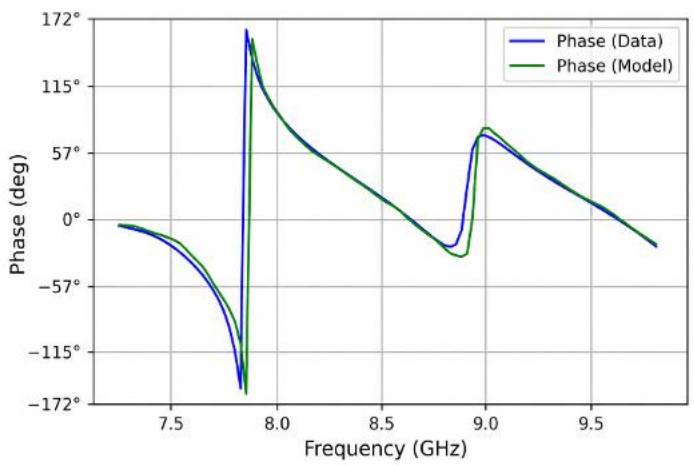

Figure 4.10: Comparison of phase from ANN predictions and HFSS simulations across frequency

The proposed Artificial Neural Network employs a hybrid activation strategy, alternating between ReLU and Sigmoid functions, and is trained using the Adam optimizer selected for its efficiency and adaptive learning capabilities. The model achieves an impressively low test error rate of just 0.012%, highlighting its robustness and precision in capturing the antenna's electromagnetic behavior. Figure 4.11 further substantiates the model's predictive accuracy by comparing the optimized return loss values against those obtained from HFSS simulations.

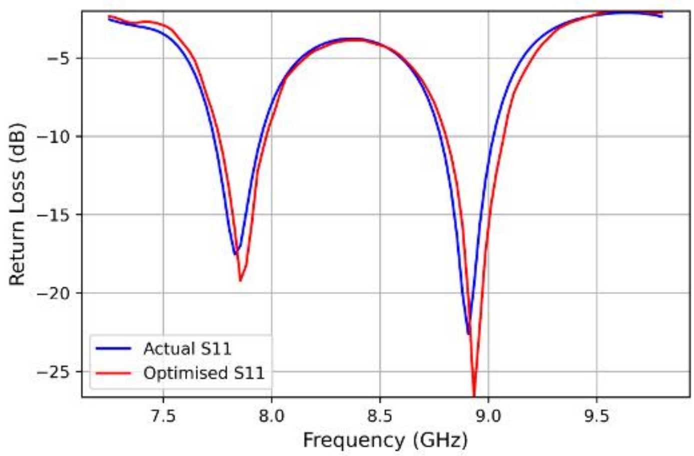

Figure 4.11: Comparison of optimized return loss from the ANN model and HFSS simulations

Additionally, as detailed in Table 4.2 presents a comparison between the proposed ANN model and previously reported works in terms of network architecture and test error performance. As observed, the General Regression Neural Network (GRNN) model reported in [71] achieved a test error of 0.41%, while the Radial Basis Function-based ANN (RBF-ANN) in [72] exhibited a significantly higher test error of 25%, indicating lower prediction accuracy. The 8-layer Sigmoid-based ANN from [73] provided a moderate improvement with a test error of 2.40%.

In contrast, the proposed model ([74]), which integrates five ReLU layers followed by three Sigmoid layers, demonstrates a remarkable reduction in test error to 0.012%. This substantial improvement highlights the effectiveness of combining ReLU and Sigmoid activation functions in enhancing model convergence and generalization. The remarkable performance of the suggested architecture confirms its robustness and high accuracy in modeling complex nonlinear relationships compared to existing ANN configurations.

Table 4.2: Comparison with state-of-the-art work

Ref	**Hidden Layers**	**Test Errors**
[71]	GRNN	0.41%
[72]	RBF-ANN	25%
[73]	8 Sigmoid	2.40%
Prop. [74]	5 ReLU + 3 Sigmoid	0.012%

5 Summary

This study presented a highly accurate ANN model developed to improve the return loss characteristics of a newly proposed antenna. The model architecture integrates two distinct activation functions, ReLU and Sigmoid, strategically deployed across its layers to enhance learning efficiency.

The input layer is designed to accept five critical parameters: feed line width, the radius of the central circular slot, the radii of eight peripheral sub-circles, and the operating frequency. The output layer produces the real and imaginary components of the return loss (S_{11}).

A dataset comprising 20,000 samples generated through comprehensive simulations in HFSS served as the foundation for model training and evaluation, with an 80/20 split utilized for training and testing, respectively. Despite the relatively modest dataset size, the model demonstrated impressive predictive accuracy and generalization capabilities.

These results underscore the ANN model's effectiveness in antenna design optimization and its promising potential for future applications in intelligent, data-driven antenna engineering.

CHAPTER 5

Performance Evaluation of a Rectangular Nested Fractal Antenna for Multiband Wireless Applications

1 Introduction

The ongoing progress in wireless communication technologies has fueled extensive research into the advancement of compact, high-capability, and application-specific microstrip antennas. Rectangular patch configurations continue to be widely used because of their simple geometry, compact structure and straightforward integration. Recent works have demonstrated the versatility of such antennas across a wide range of applications.

Ramesh Kumar Verma *et al.* [75] proposed antenna with strategically inserted notches and slots to achieve triple-band operation. Initially resonating at a single frequency, the antenna was modified to operate at 1.422 GHz, 1.791 GHz, and 2.467 GHz by introducing multiple slots, enhancing the impedance bandwidth to 1.97%, 10.35%, and 33.16%, respectively. The upper band, operating at 2.467 GHz with a S_{11} of –34.52 dB, falls within the Bluetooth spectrum (2.40–2.48 GHz), while the lower bands suit L-band wireless applications. The antenna was modeled and analyzed using IE3D simulator and fed through a 50 Ω microstrip feeding line.

Oscar Ossa-Molina *et al.* [76] presented a simplified analytical framework for calculating the key parameters of slot-loaded antennas. By analyzing the impact of slot placement on the dominant operating frequency, the model provides a quick and reliable estimation method that closely aligns with experimental and simulation data. The study demonstrated that the presence of a slot introduces minor impedance variations, slightly altering the resonant frequency while maintaining harmonic behavior similar to an un-slotted patch. The proposed model facilitates efficient antenna design through mathematical expressions that accurately describe performance shifts due to slot parameters.

Martínez-Lozano *et al.* [77] suggested a tiny ultra-wideband printed antenna tailored for examination of tissue samples and microwave healthcare imaging. Based on a modified rectangular monopole structure, the design underwent geometric optimization through parametric analysis using a 3D finite element simulator. Constructed on an economical FR4 substrate measuring 40×36 mm^2, the antenna demonstrated a broad operational frequency range spanning 2.7 GHz to 11.4 GHz. Measurements confirmed omnidirectional radiation and UWB performance. Furthermore, simulations involving four antennas placed around a breast phantom showed promising results, validating the antenna's potential for biomedical imaging applications.

Palsokar and Lahudkar [78] developed a reconfigurable antenna capable of adjusting frequency and radiation pattern with a single PIN diode to minimize circuit complexity. The antenna is capable of switching between two distinct modes and operates at resonant frequencies of 2.47 GHz, 3.8 GHz, and 5.36 GHz. By strategically placing the biasing lines positioned away from the radiating patch and utilizing a pattern-search algorithm to optimize the feed, the design ensures effective impedance matching and radiation pattern reconfiguration. These enhancements distinguish the proposed antenna from prior designs, offering versatility for dynamic wireless applications.

Douhi *et al.* [79] suggested a flexible 40×10 mm^2 antenna array made especially for wearable technology and RF energy harvesting. Operating at 5 GHz, The antenna attains a high gain. of 14.54 dBi and a bandwidth of 6.78%. The structure is entirely textile-based, employing E-shield conductive fabric with 5×10^5 S/m conductivity for the radiating and feeding elements, and a soft textile substrate for flexibility and user comfort. An inset feed technique ensures optimal impedance matching. Simulation studies of the antenna were performed using Ansys HFSS and CST MWS software, confirming its suitability for compact, low-cost, and efficient wearable RF systems.

This chapter presents a novel design concept for a rectangular nested fractal antenna that creates a distinctive nested fractal geometry by repeatedly embedding smaller rectangular patterns inside the main patch. With bandwidths up to 210 MHz, this arrangement allows the antenna to attain seven different resonant frequency bands between 1.99 GHz and 9.39 GHz, exhibiting better multiband performance than previous designs. The proposed antenna also exhibits an enhanced maximum gain of 18.86 dBi while maintaining a compact size of $40 \times 50 \times 0.8$ mm^3, guaranteeing compatibility with contemporary communication devices. By keeping a straightforward, easily fabricated structure and offering a balanced performance across several frequency bands, the design effectively addresses the limitations found in previous works. Its distinctive geometry distinguishes itself from traditional fractal arrangements by optimizing resonant mode distribution and enhancing electromagnetic coupling.

The developed antenna is applicable to a variety of modern and emerging communication technologies, , leading to high-performance approach. Firstly, the design concept and development methodology of the proposed antenna are described, including the hypothetical foundations and realization steps. Secondly, the simulation results are analyzed in detail, highlighting the performance for every design cycle and the verification of the fabricated prototype through experimental measurements. Finally, the main outcomes of this research are summarized, highlighting the novelty of the suggested design and its possible influence on cutting-edge wireless systems.

2 Antenna Design

The design of the suggested rectangular fractal antenna is based on a compact and efficient geometry intended for contemporary applications including wireless connectivity. Figure 5.1 shows a top-view layout of the final antenna configuration, highlighting its complex fractal structure and the careful choice of materials. The antenna geometry has been optimized through multiple design iterations to achieve enhanced performance across several frequency bands.

The fundamental resonant frequency of the antenna is mathematically defined by Equation (5.1) and it is primarily determined by the length L of the antenna element and the substrate's permittivity:

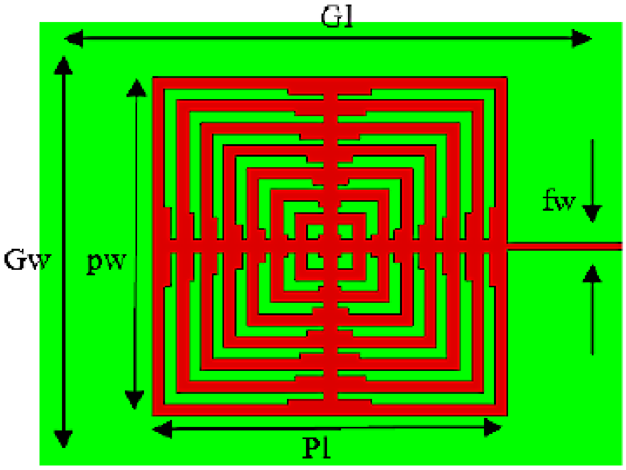

Figure 5.1: The suggested fractal antenna from above

$$f_r = \frac{c}{2L\sqrt{\varepsilon_r}} \tag{5.1}$$

where

- c is the speed of light in free space (3×10^8 m/s),
- L corresponds to the actual length of the patch,
- ε_r is the relative permittivity of the substrate material.

This formula assumes that the antenna behaves like a half-wavelength resonator in the permittive medium.

The width w of the patch affects the input impedance and bandwidth. It is chosen to maximize the radiation efficiency and bandwidth, is expressible in the form of in analytical form as in Equation (5.2):

$$w = \frac{c}{2f_r\sqrt{\varepsilon_{\text{eff}}}} \tag{5.2}$$

where ε_{eff} is expressed quantitatively in Equation (5.3) and it is the overall dielectric constant, accounting for fringing fields which make the wave partly travel in air and partly in the substrate.

Since the fields are not confined completely to the substrate but fringe into the air, the effective dielectric constant is less than the substrate dielectric constant:

$$\varepsilon_{\text{eff}} = \frac{\varepsilon_r + 1}{2} + \frac{\varepsilon_r - 1}{2}\left(1 + 12\frac{h}{w}\right)^{-\frac{1}{2}} \tag{5.3}$$

where

- h is the height of the substrate,
- w is the patch width.

This empirical formula approximates the combined effect of the substrate and air.

Due to fringing effects, the patch's electrical length exceeds its physical length which can be described using Equation (5.4):

$$L_{\text{eff}} = \frac{c}{2f_r\sqrt{\varepsilon_{\text{eff}}}} \tag{5.4}$$

The extra length caused by fringing fields on each side of the patch is expressed quantitatively in Equation (5.5):

$$\Delta L = 0.412h \frac{(\varepsilon_{\text{eff}} + 0.3)\left(\frac{w}{h} + 0.264\right)}{(\varepsilon_{\text{eff}} - 0.258)\left(\frac{w}{h} + 0.8\right)} \tag{5.5}$$

This correction must be subtracted from the effective length to find the physical patch length.

Finally, the real dimension of the patch can be modeled as given in Equation (5.6):

$$L = L_{\text{eff}} - 2\Delta L \tag{5.6}$$

This accounts for the fringe effects occurring at the patch extremities

The progressive evolution of the antenna's geometry is thoroughly depicted in Figure 5.2, which outlines the sequential modifications implemented throughout the design process. Each iteration introduces specific structural changes designed to enhance the antenna's operational bandwidth and radiation properties. This iterative method allows the development of a tiny yet high-performing multiband antenna.

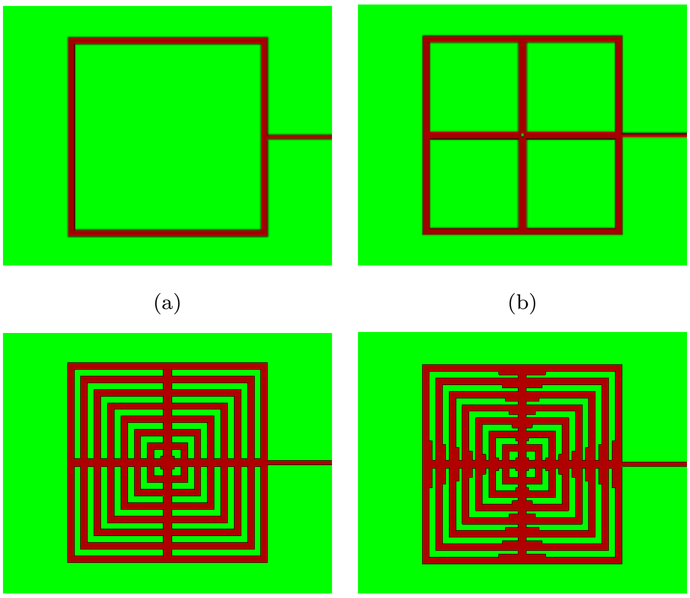

(a) (b) (c) (d)

Figure 5.2: Fractal antenna design evolution: (a) starting iteration, (b) first iteration, (c) second iteration, (d) third iteration

The antenna is fabricated on a widely available and inexpensive FR-4 substrate, selected for its appropriate dielectric properties and economic feasibility. The properties of the substrate include a ε_r of 4.7, a $\tan\delta$ of 0.02, and a thickness of 0.8 mm. The metallic layer used for radiation and signal transmission is copper with a uniform thickness of 35 μm, offering stable enhanced conductivity with minimal energy dissipation.

The top view of the manufactured layout is depicted in Figure 5.3, confirming the successful realization of the design with accurate dimensional and structural conformity to the simulated model.

As detailed in Table 5.1, the final antenna structure maintains compact overall size of 40 mm in length, 50 mm in width, and 0.8 mm in total height. These reduced dimensions make The antenna is suitable for incorporation into portable

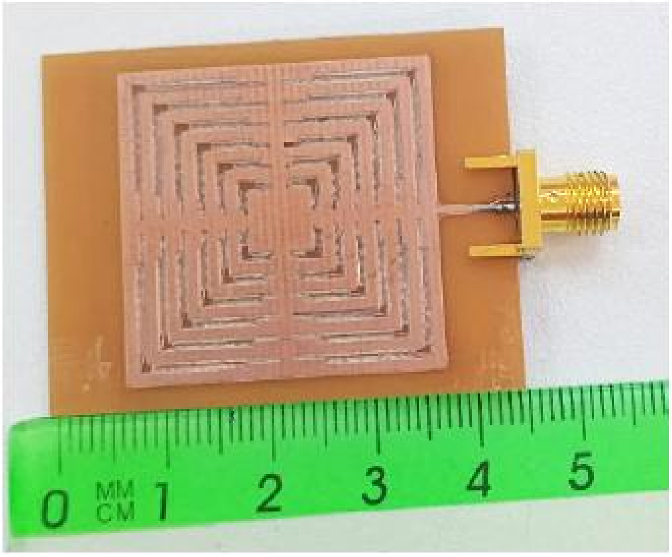

Figure 5.3: Top view of the fabricated antenna

and space-constrained devices.

Despite its small footprint, the antenna demonstrates excellent performance over multiple frequency bands, validating the capability of the fractal structure approach in attaining both size reduction and high efficiency.

Table 5.1: Optimized dimensions of designed antenna

Variables	Gw	Gl	Pw	Pl	Fw
Values (mm)	50	40	30	30	0.6

3 Results and Discussions

The electromagnetic performance of the proposed antenna design was thoroughly investigated using Ansys HFSS, due to its accuracy in high-frequency antenna modeling. This section introduces the simulation results obtained for the hexagonal fractal antenna, with a particular emphasis on critical performance metrics such as return loss, VSWR, surface current distribution, realized gain, and far-field radiation characteristics.

3.1 Return Loss and VSWR

Return loss, represented by the scattering parameter S_{11}, is a fundamental metric to analyze antenna behavior, as it quantifies the proportion of incident power reflected back at the input port. Efficient antenna operation is generally characterized by S_{11} values below –10 dB, which indicates low reflection and effective impedance matching.

The frequency-dependent return loss behavior across different design stages is illustrated in Figure 5.4, demonstrating the progressive enhancement in resonant characteristics through the iterative design process.

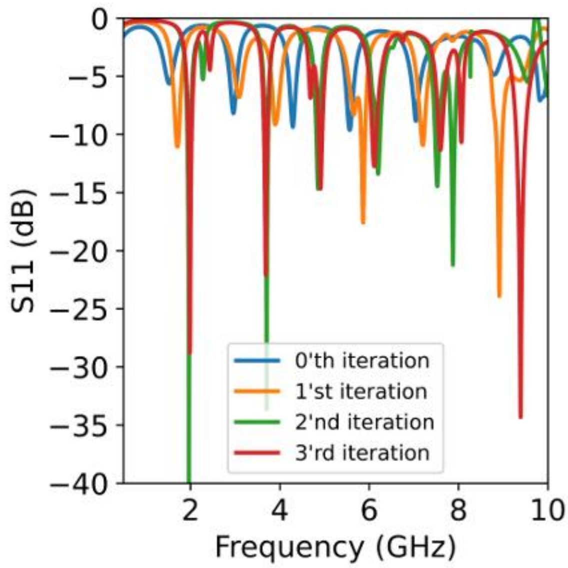

Figure 5.4: Return loss versus frequency: evaluation across all design iterations

The measured return loss covering a frequency range from 1 GHz to 10 GHz with a fine resolution of 0.001 GHz. The antenna demonstrates resonant behavior at 1.99, 3.68, 4.91, 6.11, 7.60, 8.06, and 9.39 GHz, achieving return loss values of –28.76, –22.06, –14.66, –12.73, –11.33, –10.67, and –34.30 dB, respectively. These resonances correspond to bandwidths of 90, 80, 90, 100, 70, 22, and 210 MHz, indicating a strong multiband response.

The comparison between simulated and experimental results, as depicted in Figure 5.5, confirms the precision and reliability of the proposed design across its operating bands.

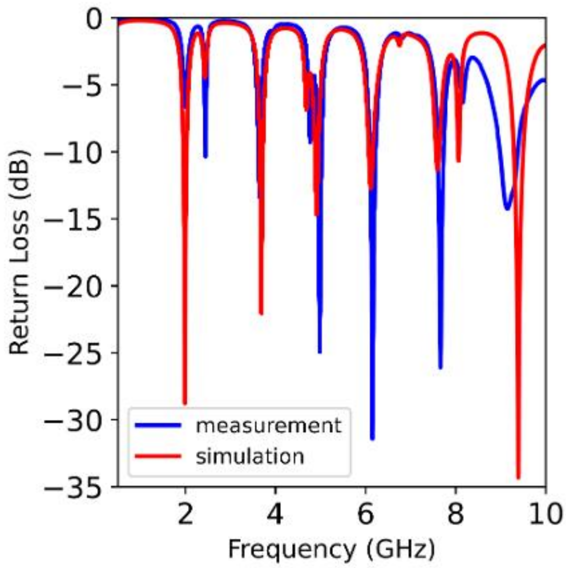

Figure 5.5: Return loss versus frequency: comparison of measured and simulated antenna responses

VSWR is an essential factor used to evaluate the impedance matching characteristics of an antenna. An ideal VSWR value is 1, reflecting excellent matching among the antenna and the feed line, thereby minimizing reflected power.

Figure 5.6 displays the simulated VSWR response of the presents rectangular nested fractal antenna across its operating frequency range. The VSWR values at the identified frequencies are 1.07, 1.17, 1.45, 1.06, 1.74, 1.82, and 1.03 all falling well within the acceptable range of 1 to 2.

These results confirm the antenna's superior impedance matching and suitability for multiband operation.

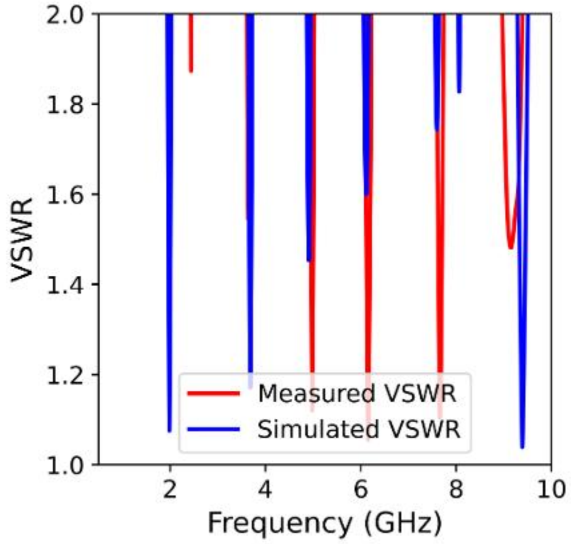

Figure 5.6: VSWR plot of the proposed antenna

3.2 Gain

The gain performance of the proposed rectangular fractal antenna was thoroughly evaluated across its resonant frequencies, demonstrating notable enhancement in radiation efficiency. The antenna attained a maximum gain of 18.86 dBi at 4.91 GHz, with corresponding gain values of 0.88, 2.18, 18.86, 8.89, 13.22, 12.24, and 4.01 dBi at 1.99, 3.68, 4.91, 6.11, 7.60, 8.06, and 9.39 GHz, respectively.

These results indicate strong radiation properties throughout a wide frequency interval, confirming the antenna's suitability for multiband and high-gain applications. Figure 5.7 illustrates the gain characteristics at the main resonant frequencies for both $\phi = 0°$ and $\phi = 90°$ cuts, providing insight into the antenna's directional behavior and consistency across different planes.

The consistently high gain values not only meet but in some instances exceed standard performance expectations for communication systems, making the design an excellent candidate for use in applications such as telecommunications, satellite links, and radar systems. The antenna's robust performance is attributed to the integration of advanced geometrical features and optimized material selection, which collectively contribute to its enhanced radiation efficiency and structural stability.

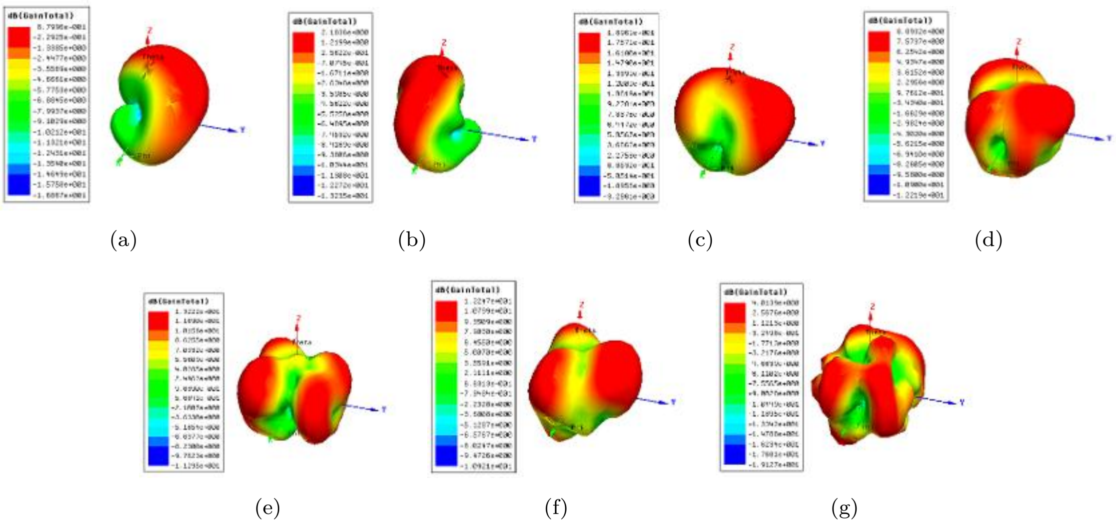

Figure 5.7: Characteristics of gain of the rectangular fractal antenna at : (a) 1.98GHz, (b) 3.68GHz, (c) 4.91GHz, (d) 6.11GHz, (e) 7.59GHz, (f) 8.06GHz, (g) 9.39GHz

3.3 Surface Current Distribution

The surface current distribution on the radiating element is crucial in understanding the electromagnetic behavior of the antenna at various frequencies. It provides detailed insight into the areas of high and low current density, which significantly contributes to the optimization of both design and performance.

Figure 5.8 illustrates the surface current distribution of the suggested rectangular fractal antenna at its resonant frequencies for $\phi = 0°$ and $\phi = 90°$ planes. These plots clearly demonstrate how the current intensity varies across different regions of the patch at each frequency.

Examining the current distributions allows detection of areas with elevated current density, facilitating focused adjustments to enhance radiation characteristics, expand bandwidth, and enhance overall gain. Moreover, this analysis supports efforts to reduce conduction and dielectric losses, thereby increasing efficiency and reliability in communication systems.

Analyzing surface current patterns also aids in achieving improved impedance matching, minimizing signal reflection and maximizing power transfer. This knowledge is particularly valuable in reducing unwanted emissions and interference, ensuring stable antenna operation even under varying environmental conditions.

Table 5.2 offers a comparative overview of the proposed rectangular nested fractal antenna against several previously published designs in terms of physical size, resonating frequencies, bandwidth, and return loss (S_{11}). A critical examination of this data underscores the high performance and compactness of the suggested antenna.

In terms of physical dimensions, the proposed design measures 40×50 mm^2,

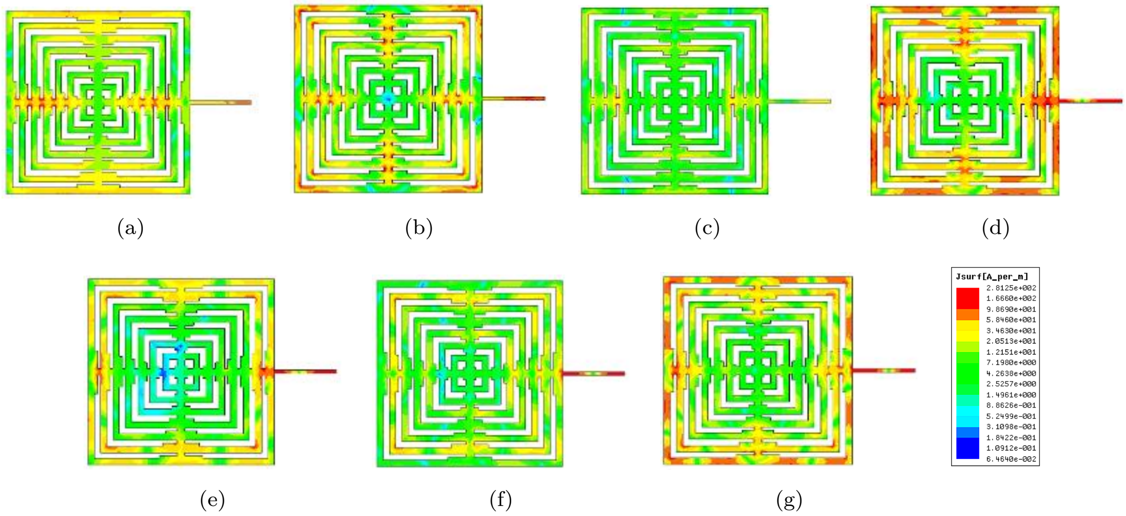

Figure 5.8: Surface current distribution of the proposed antenna at different resonant frequencies: (a) 1.98GHz, (b) 3.68GHz, (c) 4.91GHz, (d) 6.11GHz, (e) 7.59GHz, (f) 8.06GHz, (g) 9.39GHz;

providing a compact footprint relative to standard designs of other works in the literature. For instance, references [76], [78], and [79] employ significantly larger antennas (74×76 mm^2, 66×58 mm^2, and 75×47 mm^2, respectively), yet offer fewer operating bands and limited bandwidth performance. Although the design in [77] has a slightly smaller footprint (36×40 mm^2), it restricted to two bands, thereby limiting its suitability for multiband designs

One of the key strengths of the suggested antenna lies in its multiband functionality, supporting seven distinct resonant frequencies. This significantly outperforms all compared designs, most of which operate in only one to three frequency bands. Additionally, the proposed antenna exhibits broad bandwidths at each resonance, ranging from 22 MHz to 210 MHz. In contrast, bandwidths in other designs tend to be narrower or inconsistent across bands.

The return loss (S_{11}) values of the proposed antenna also reflect strong impedance matching at all operating frequencies. The antenna achieves return losses as low as –34 dB, with all resonant frequencies maintaining S_{11} values below –10 dB, satisfying the general performance criterion for efficient radiation. Compared to the referenced works, which show return losses between –12 dB and –32 dB, the proposed antenna performs equally well or better, particularly considering the broader operating spectrum.

Table 5.2: Comparison of the proposed antenna's performance against previously published rectangular antennas

Ref	Size (mm^2)	No. Bands	BW (MHz)	S_{11} (dB)
[75]	47×39	3	28, 188, 813	-18, -12, -34
[76]	74×76	3	50, 70, 100	-32, -12, -13
[77]	36×40	2	2400, 11400	-30, -20
[78]	66×58	3	50, 20, 40	-16, -15, -13
[79]	75×47	1	170	-28
Prop. [80]	40×50	7	90, 80, 90, 100, 70, 22, 210	-28, -22, -14, -12, -11, -10, -34

4 Summary

This chapter presented the experimental validation of a novel rectangular nested fractal antenna with small footprint of 40 × 50 mm^2. The antenna demonstrated multiband operation, with resonant frequencies observed at 1.98, 3.68, 4.91, 6.11, 7.59, 8.06, and 9.39 GHz. A peak gain of 18.96 dBi was achieved, indicating high radiation efficiency.

The simulated results showed strong agreement with measured data from the fabricated prototype, confirming reliable performance across the targeted bands. The antenna exhibited stable radiation patterns in both the vertical and horizontal planes, along with favorable impedance matching characterized by

VSWR values consistently below 2.

In comparison with traditional rectangular patch antennas, the suggested design offers enhanced gain and broader frequency coverage, making it an attractive candidate for advanced wireless communication, radar, and satellite systems.

CHAPTER 6

Automated Design and Performance Optimization of Inverted Sierpinski Fractal Crossed Bowtie Antennas for Multiband Wireless Applications

1 Introduction

Fractal geometries are distinguished by their space-filling capabilities and self-similarity, have garnered significant attention in antenna engineering for their ability to achieve compact, multiband, and broadband performance. These features are especially beneficial in modern wireless systems where antenna miniaturization and frequency reconfigurability are critical.

Sierpinski-based structures are among the most extensively explored fractal geometries due to their recursive nature and suitability for multiband behavior. Clower *et al.* [81] developed a 3D-printed Tetrahedral antenna based on the Sierpinski gasket fractal geometry using graphene composites to achieve wideband and multifrequency performance. Two fabrication methods were explored: coated ABS and graphene-impregnated PLA. Simulations and experiments showed strong performance with over 35 dB return loss at resonance, demonstrating the potential of additive manufacturing for compact, multi-band antenna designs.

Masroor *et al.* [82] presented a Sierpinski-carpet fractal microstrip patch antenna with frequency reconfigurability is proposed for Ku, K, and Ka band applications. The design incorporates a PIN diode, modeled as a lumped RC component in HFSS, to enable reconfigurable operation. The compact antenna (9.5×7.4 mm^2) was both simulated and experimentally validated, demonstrating high impedance bandwidth and effective performance across multiple frequency bands, thereby enhancing its suitability for contemporary wireless communication systems. Singhal [83] proposed an ultra-wideband terahertz antenna featuring a square-shaped third-iteration Sierpinski Carpet asymmetrically fed radiator powered by a modified coplanar waveguide (CPW) structure. Operating across 2.2–10.5 THz with a VSWR $\leq$ 2, the antenna demonstrates a compact footprint ($42\,\mu$m $\times$ $22\,\mu$m $\times$ $1.6\,\mu$m) and a highest obtained realized gain of 5.5 dBi. Its wide bandwidth, compact design, and stable radiation performance make it well-suited for terahertz and high-speed communication applications.

Al-Khafaf *et al.* [84] conducted a performance comparison between conventional wideband bowtie antennas and Sierpinski-based fractal multiband bowtie designs. By introducing self-similar geometries into the traditional bowtie structure, they achieved frequency reconfigurability and multiband operation at 2.4, 9.2, and 17.4 GHz. Three antenna types a dipole, a broadband bowtie, and a Sierpinski fractal bowtie were designed and analyzed using MATLAB and CST simulations. The study demonstrated that the fractal bowtie antenna maintains desirable return loss, gain, and directivity while offering the flexibility of compact multiband functionality, thus making it a viable candidate for reconfigurable wireless communication platforms.

Sanu *et al.* [85] investigated the use of fractal geometries to enhance microstrip antennas for Wi-Fi applications, focusing on achieving antenna miniaturization, enhanced multiband performance, and reduced cross-polarization. Four fractal geometries Sierpinski carpet, Sierpinski gasket, circular patch, and Koch were designed and analyzed up to the third iteration using FR4 epoxy substrates. The Koch fractal antenna at the third iteration achieved the best performance, with a return loss of −39.85 dB and a gain of 3.6 dB at 5.2 GHz. To suppress cross-polarization, a square slot was incorporated into the feed line, resulting in a reduction of up to 60 dB. Simulations conducted in *Ansys HFSS* validated the antenna's directional radiation pattern and its suitability for 5 GHz wireless communication applications.

Kaushal *et al.* [86] proposed and analyzed modified planar feed Sierpinski gasket fractal antennas for multiband vehicular applications. To address reflection issues observed in classical and perturbed gasket geometries, the authors introduced a novel design using metamaterial-engineered substrates. These substrates not only minimized reflections across multiband frequencies but also enabled frequency lowering and antenna miniaturization. Experimental validation confirmed the efficiency of the suggested method, which makes it a viable option for small, adaptable car antenna systems.

Rao [87] proposed a modified Sierpinski fractal geometry to improve miniaturization in triangular microstrip patch antennas compared to the conventional Sierpinski design. Implemented on a Rogers RO4003 lossy substrate ($\varepsilon_r = 4.3$), the design achieves over 50% size reduction, with fractalization carried out up to the fourth iteration. A comparative analysis between conventional and modified geometries was conducted using simulations of S_{11} and radiation patterns, demonstrating enhanced miniaturization without compromising performance, making the design suitable for compact wireless applications.

In this chapter, the design, optimization, and performance analysis of an inverted Sierpinski fractal antenna in the form of crossed bowties are presented. Despite the extensive research on modified Sierpinski fractal antennas and their hybridizations with other geometries, the concept of the inverted Sierpinski configuration, particularly using crossed bowtie structures, remains largely unexplored. To address this research gap, a third-iteration crossed bowtie structure based on an inverse Sierpinski gasket fractal is proposed and optimized for enhanced radiation performance.

The novelty of this work lies in the use of an inverse Sierpinski geometry, realized through a crossed bowtie arrangement that ensures a more uniform current distribution across the radiating patch compared to conventional designs. To achieve precise geometric alignment and improved current flow, Python scripting was employed to accurately overlap all fractal components. The proposed antenna operates within the 0–6 GHz frequency range, covering multiple FCC-regulated bands that support various modern wireless technologies. This wide operating range makes the antenna well-suited for applications such as WLAN, IoT, and 5G systems, while maintaining regulatory compliance and minimizing electromagnetic interference. Firstly, the design concept and iterative development process of the proposed inverted Sierpinski crossed bowtie antenna are described. Secondly, the parametric analysis and performance evaluation are presented and discussed, highlighting the effect of geometric variations on the antenna's characteristics. Finally, the main results are summarized, emphasizing the originality, effectiveness, and potential applications of the proposed design in advanced wireless communication systems.

2 Antenna Design

The proposed antenna utilizes an inverted Sierpinski triangle geometry, created through iterative removal of smaller triangles from a larger equilateral triangle. This fractal approach enhances multiband behavior and achieves significant size reduction. A crossed bowtie structure based on this geometry up to the third iteration was designed using Python scripting, ensuring accurate element alignment and continuous current flow.

The proposed antenna is fabricated on an FR4 epoxy substrate characterized by a relative permittivity of $\varepsilon_r = 4.4$, a substrate thickness of 1.6 mm, and total physical dimensions of 90×100 mm^2. Simulations were conducted using ANSYS HFSS v22 to analyze return loss, surface currents, and radiation characteristics.

The final antenna layout, including the top view and detailed structure, is depicted in Figure 6.1(a) and Figure 6.1(b). The fractal development through successive iterations is shown in Figure 6.2(a–d), from the first to the fourth stage.

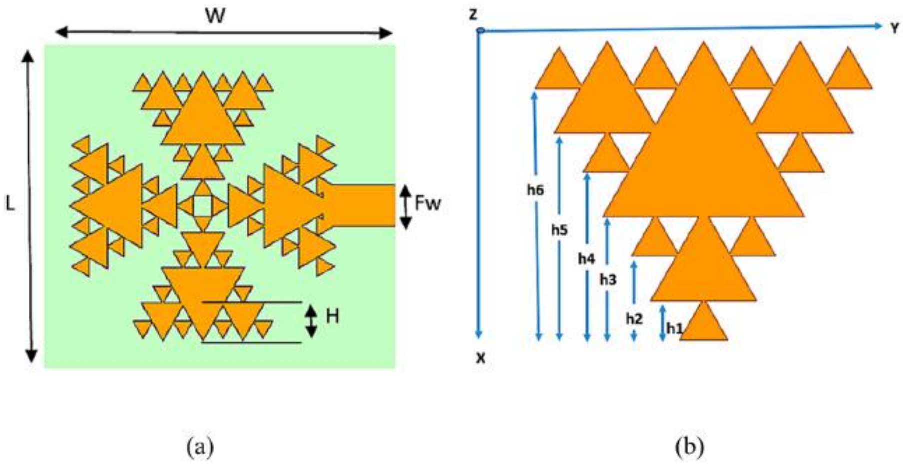

Figure 6.1: Top view illustrating the geometry of the proposed antenna, and (a) Detailed structural configuration of the proposed antenna (b)

Side dimension of the triangular element at the nth iteration can be represented in mathematical form by Equation (6.1):

$$L_n = L_0 \times 2^n \tag{6.1}$$

where L_0 denotes the side dimension of the initial triangular structure, and n represents the corresponding iteration order.

Total count of triangular sections eliminated during the n^{th} iteration can be described using Equation (6.2):

$$N_n = 3^n \tag{6.2}$$

This denotes the overall quantity of smaller triangular elements eliminated after n iterations.

Fraction of the surface area eliminated during the n^{th} iteration can be mathematically formulated as shown in Equation (6.3):

$$A_n = \left(\frac{3}{4}\right)^n \tag{6.3}$$

This equation expresses the proportion of the surface area eliminated after the n^{th} iteration.

Cumulative surface area eliminated after n iterations can be described using Equation (6.4):

$$A_t = \sum_{k=1}^{n} N_k \times A_k = L_0^2 \times \left(\frac{3}{4}\right) \times \left(1 - \left(\frac{3}{4}\right)^n\right) \tag{6.4}$$

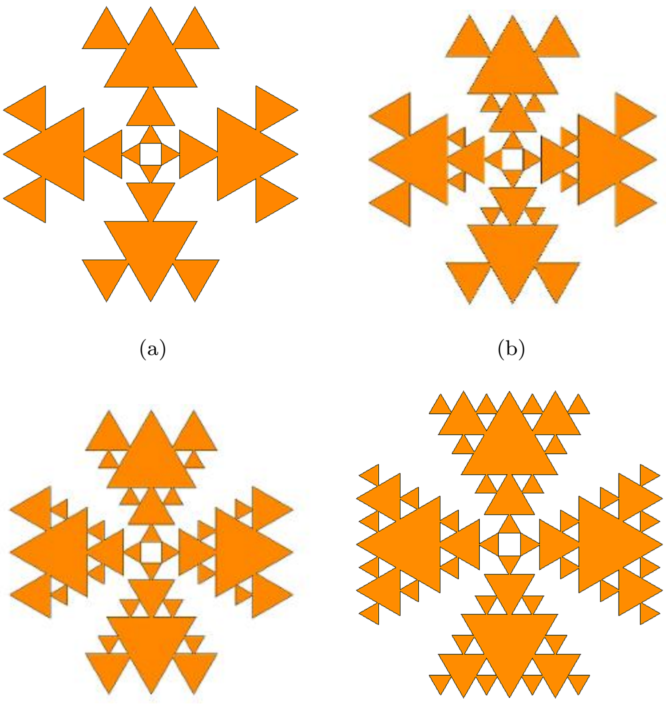

(a) (b) (c) (d)

Figure 6.2: The suggested antenna geometry is as follows: (a) initial iteration, (b) subsequent iteration,(c) The third iteration; (d) The fourth

This equation can be modeled as given in (6.5): determines, after n iterations, the total area taken out of the initial triangle.

Width of the bowtie element:

$$W = L_0 \times \cos\left(\frac{\pi}{6}\right) = L_0 \times \frac{\sqrt{3}}{2} \tag{6.5}$$

This equationrepresents The bowtie width, created by the intersection of two Sierpinski triangular sections, defines the overall radiating span of the structure. The effective length of the bowtie, which determines the resonant frequency behavior of the antenna, can be expressed as in Equation (6.6):

$$L_{\text{eff}} = 2 \times L_0 \times \left(1 - \frac{1}{2^n}\right) \tag{6.6}$$

The physical realization of the antenna is depicted in Figure 6.3, showing the top view of the fabricated prototype with clearly defined fractal edges and a well-aligned feed structure, consistent with the simulated design. This prototype was developed on an FR4 substrate using standard PCB fabrication techniques to verify the simulated performance in practice. All dimensional parameters used during fabrication are provided in Table 6.1.

Table 6.1: Dimensions of the suggested antenna

Variables	W	L	fw	H	h1	h2	h3	h4	h5	h6
Values (mm)	100	90	8.9	17	3.5	7.85	11	15	18.85	22.85

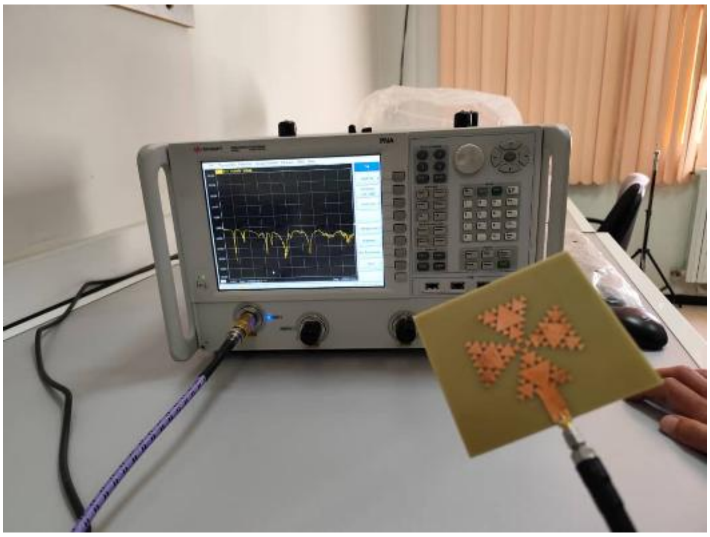

Figure 6.3: Measurement of the proposed antenna using VNA

3 Results and Discussions

This section presents the simulation, modeling, fabrication, and measurement results of the proposed crossed bowtie antenna based on the inverted Sierpinski fractal geometry. Key performance parameters including return loss, gain (in dBi), surface current distribution, Smith chart characteristics, and radiation pattern behavior are comprehensively analyzed. The antenna was fabricated on an FR4 substrate with a thickness of 1.6 mm, a relative permittivity of $(\varepsilon_r = 4.4), andacoppercladdingthicknessof 0.035\ mm.$

3.1 Return Loss

The performance of the suggested antenna with FR4 as the substrate material is shown in Figure 6.4. In comparison to other dielectrics like Teflon, polyimide, and Rogers RT/Duroid 5880, FR4 has more resonant frequency ranges and better return loss properties. Its dielectric constant and loss tangent work together to greatly increase multi-band performance, which is responsible for this enhancement.

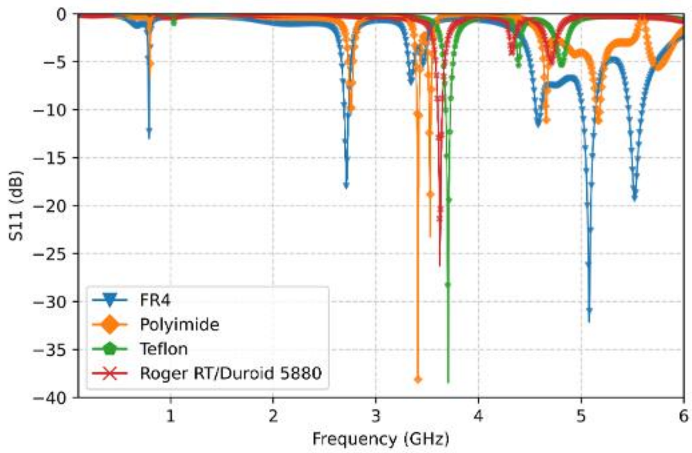

Figure 6.4: Impact of dielectric material on the performance of antennas

Figure 6.5 investigates how the antenna's return loss is affected by the feed line placement and resonant behavior. Notably, shifting the feed location causes a rightward frequency displacement and degradation in return loss, highlighting that optimal feed placement is critical for achieving desired impedance matching and bandwidth performance. The observed rightward frequency shift in non-FR4 materials further emphasizes the design's sensitivity to both dielectric properties and feed configuration.

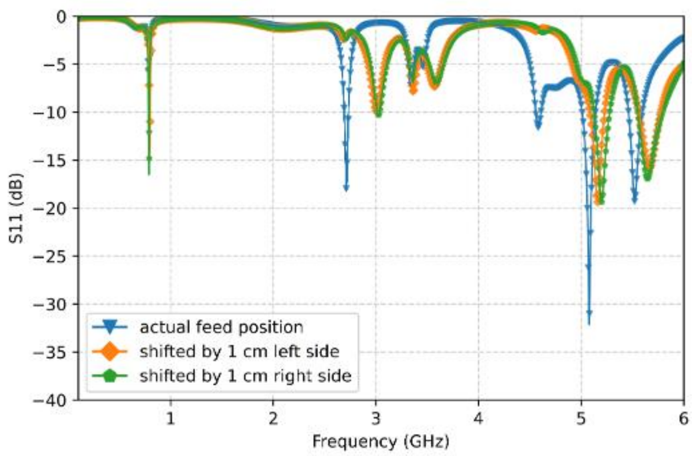

Figure 6.5: Effect of feed position on antenna performance

In Figure 6.6, the antenna's response to a feed width of 0.89 cm is presented, demonstrating an increase in the number of supported resonant bands. While variations in feed width do not significantly alter the resonant frequency positions, they notably affect return loss levels, suggesting that feed width primarily affects impedance matching instead of frequency tuning.

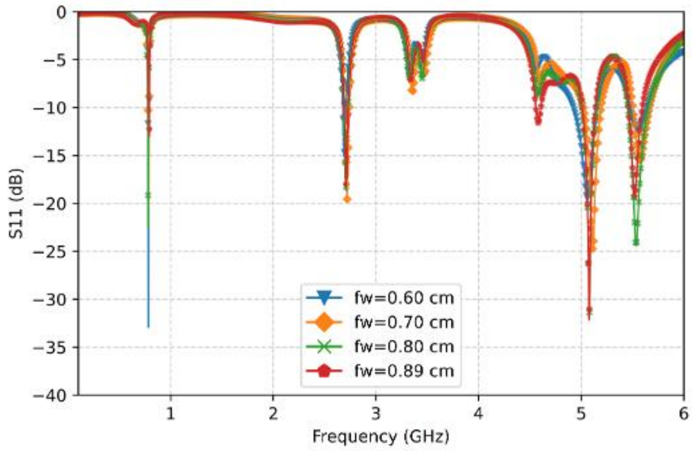

Figure 6.6: The impact of feed width on antenna efficiency

Finally, Figure 6.7 explores the the ground plane length's impact on antenna efficiency. Although variations in ground length do not result in drastic changes, a ground length of 10 cm emerges as optimal, providing a balanced trade-off between extended frequency coverage and consistent return loss behavior.

Figure 6.8 depicts the evolution of the return loss characteristics across successive iterations of the antenna design. In the zero iteration (blue curve), two resonant frequencies are observed at 2.45 GHz and 4.73 GHz, with corresponding return losses of –13 dB and –21 dB. The first iteration (orange curve) exhibits resonances at 0.85 GHz and 5.65 GHz, achieving return losses of –10 dB and –12 dB. The second iteration (green curve) shows an enhanced response, with

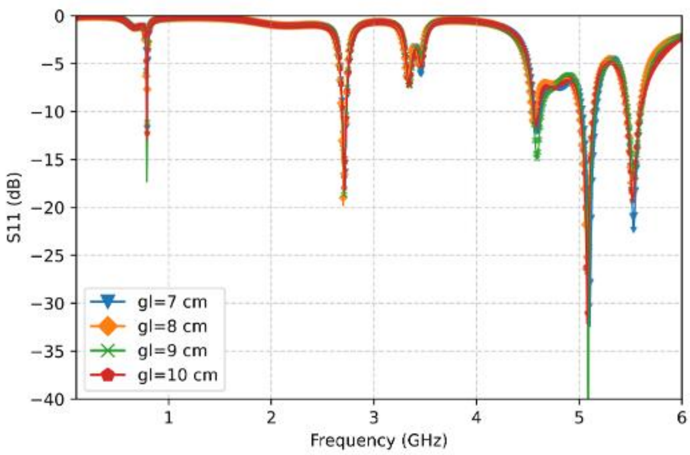

Figure 6.7: Effect of ground plane length on antenna performance

resonant frequencies at 0.92 GHz and 5.80 GHz and return losses of –13 dB and –10 dB, respectively. The third iteration (red curve) demonstrates the most refined multiband performance, featuring five distinct resonant frequencies at 0.79 GHz, 2.71 GHz, 4.58 GHz, 5.08 GHz, and 5.52 GHz, with corresponding return losses of –13 dB, –18 dB, –11 dB, –32 dB, and –19 dB, respectively.

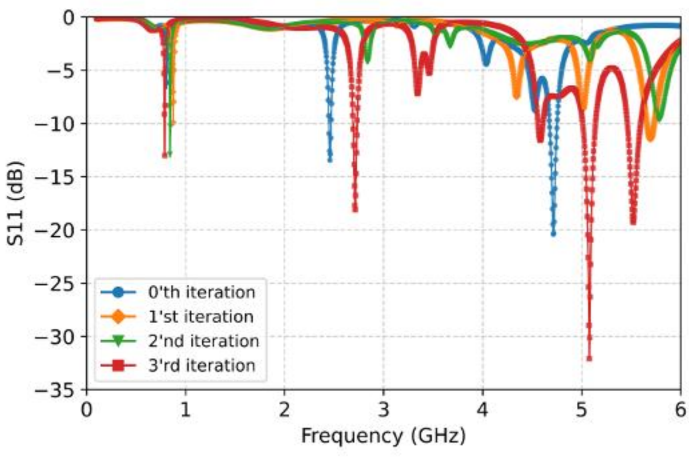

Figure 6.8: Return loss characteristics of every iteration

As illustrated in Figure 6.9, the fabricated antenna was tested using a 50 Ω SMA connector and characterized with a vector network analyzer (VNA). The measured outcomes exhibit strong agreement with the simulated results. The first measured resonance occurs at 0.75 GHz with a return loss of –11 dB, compared to the simulated value of 0.79 GHz (–13 dB). The second measured band appears at 2.65 GHz (–13 dB), closely matching the simulated 2.71 GHz (–18 dB). Although the simulation indicates minor resonances near 3.5 GHz (–7 dB and –5 dB), these do not meet the –10 dB criterion. The fourth and fifth measured bands are observed at 5.20 GHz (–25 dB) and 5.60 GHz (–17 dB), showing good correspondence with the simulated resonances at 5.08 GHz (–32 dB) and 5.52 GHz (–19 dB), respectively.

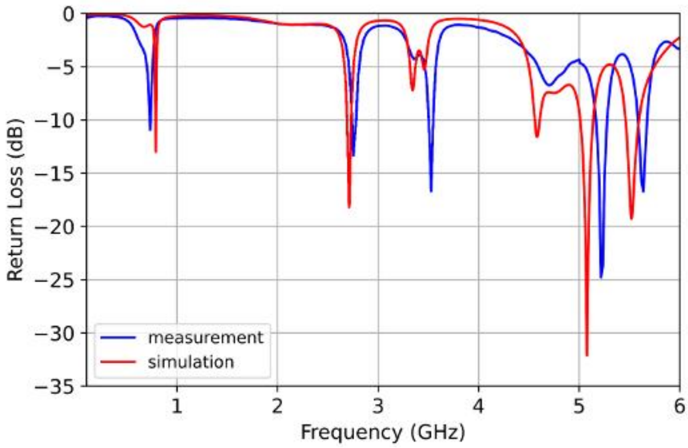

Figure 6.9: Measured return loss vs simulated return loss

3.2 Gain

Figure 6.10 illustrates the gain performance of the proposed antenna, which serves as a crucial metric for assessing its overall efficiency. At the resonant frequencies of 2.75 GHz, 3.53 GHz, 5.22 GHz, and 5.64 GHz, the antenna achieves gain levels of 0.47 dBi, 6.82 dBi, 8.73 dBi, and a maximum of 13.47 dBi, respectively. The peak gain of 13.47 dBi demonstrates the antenna's high radiative efficiency and confirms its effectiveness for reliable operation across multiple frequency bands in advanced multiband communication systems.

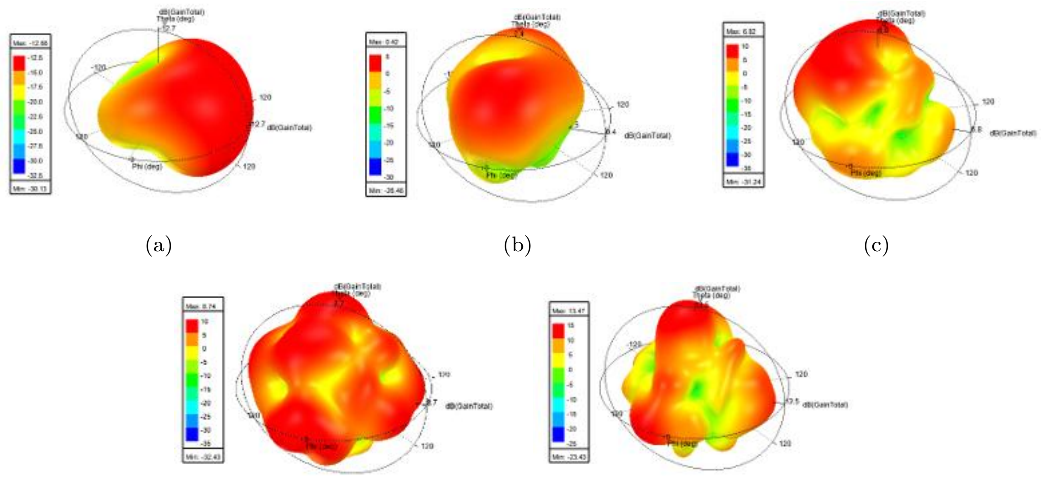

(a) (b) (c) (d) (e)

Figure 6.10: Gain of the proposed antenna at each resonating frequency: (a) 0.79 GHz, (b) 2.71 GHz, (c) 4.58 GHz, (d) 5.08 GHz, (e) 5.52 GHz

3.3 Surface Current Distribution

Figure 6.11 illustrates the surface current distribution of the proposed antenna at its resonant frequencies of 0.79 GHz, 2.71 GHz, 4.58 GHz, 5.08 GHz, and 5.52 GHz. At 0.79 GHz, the surface current is widely distributed across the radiating patch, with higher intensity observed near the feed point and along the main edges. As the operating frequency increases, the current becomes more localized, especially along the triangular boundaries of the fractal structure, indicating the excitation of higher-order resonant modes. At higher frequencies (4.58 GHz and above), the current density is primarily concentrated around the sharp corners and junctions, reflecting efficient radiation at these frequencies. This behavior highlights the effectiveness of the fractal bowtie geometry in enabling multiband operation through enhanced resonance across multiple frequency bands.

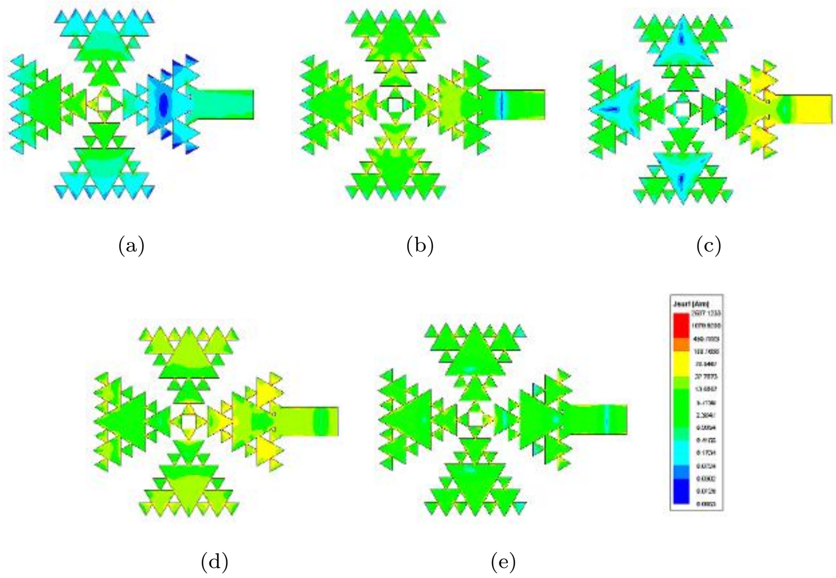

Figure 6.11: Surface current distribution at each resonating frequency: (a) 0.79 GHz, (b) 2.71 GHz, (c) 4.58 GHz, (d) 5.08 GHz, (e) 5.52 GHz

Table 6.2 presents a comparative analysis of the proposed antenna (Ref. [88]) with previously reported designs in terms of the number of resonant frequency bands and their corresponding maximum gain values. The proposed antenna exhibits enhanced multiband behavior and improved gain performance. In contrast to earlier designs, it successfully achieves five distinct resonant frequencies (0.79, 2.71, 4.58, 5.08, and 5.52 GHz), which is the highest among all listed references. In contrast, most prior works (Refs. [81], [83], [84], and [89]) report tri-band behavior, while others (Refs. [82], [85], and [87]) are limited to single-band or dual-band operations. Additionally, the proposed design exhibits a peak gain of 13.47 dBi, significantly outperforming the other antennas in the table. For instance, Ref. [86] comes closest in terms of gain, with a peak of 10.6 dBi across four bands, but it still falls short of both the gain and number of operating bands achieved by the proposed structure. Other works report much lower gains, ranging from 1.77 dBi (Ref. [84]) to 7.35 dBi (Ref. [83]). This notable enhancement in both gain and frequency diversity is primarily attributed to the optimized inverted Sierpinski fractal bowtie geometry and its third-order iteration, which enables efficient radiation at multiple bands without compromising gain. Moreover, the careful tuning of design parameters such as feed position, ground plane size, and fractal iteration further contributes to this improved performance. Hence, the proposed antenna not only supports a greater number of usable frequency bands, but it also offers better radiation efficiency, making it particularly suitable for advanced multiband wireless applications that demand both compact design and high gain performance.

Table 6.2: Comparison of the proposed antenna with existing related antennas in literature

Ref	**No. Bands**	**Resonant Frequencies (GHz)**	**Maximum Gain (dBi)**
[81]	3	2.41, 6.59, 9.8	4.19
[82]	1	2.45	4.5
[83]	2	2.5, 3.4	7.35
[84]	3	2.4, 9.2, 17.4	1.77
[85]	1	5.2	2.5
[86]	4	0.48, 1.41, 2.32, 3.88	10.6
[87]	1	3.1, 12.5	3.16
[89]	3	4.23, 4.63, 6.39	6.82
Prop. [88]	5	0.79, 2.71, 4.58, 5.08, 5.52	13.47

4 Summary

This chapter has detailed the development, simulation, and fabrication of a novel inverted Sierpinski fractal antenna featuring a crossed bowtie design with overall dimensions of 90 × 100 mm^2. The antenna exhibits clear multiband behavior, resonating effectively at 0.75, 2.65, 3.5, 5.20, and 5.52 GHz, and achieves a peak gain of 13.47 dBi. Simulated outcomes were closely validated through experimental testing of the fabricated prototype, with radiation patterns displaying strong performance across both principal planes. The VSWR remained below 2 at all resonant frequencies, indicating good impedance matching. Compared to existing Sierpinski-based antennas, the proposed design offers enhanced multiband operation and superior gain characteristics. Its performance makes it a strong candidate for various wireless communications.

CHAPTER 7

Conclusions and Suggestions for Further Work

1 Conclusions and Suggestions for Further Work

This research focused on the study, design, optimization, fabrication, and experimental evaluation of compact multiband microstrip antennas based on fractal geometries. Several innovative fractal antenna configurations were proposed to meet the growing requirements of modern wireless communication and radar systems for compact, efficient, and high-performance antenna solutions.

In the first part, a hybrid wheel-shaped antenna integrating Sierpinski carpet and Koch snowflake fractal geometries was developed to achieve five-band operation with high gain and wide impedance bandwidth, making it suitable for various applications, including Wi-Fi, 5G, radar, satellite, and Bluetooth communication systems.

In the second part, a modified Apollonian gasket fractal antenna was optimized using an artificial neural network (ANN) model to improve its return loss and impedance matching characteristics in the upper microwave frequency range. This AI-assisted approach demonstrated the potential of machine learning techniques in enhancing the electromagnetic performance of complex fractal antenna designs.

In the third part, a compact rectangular nested fractal antenna was designed, fabricated, and experimentally validated to cover seven distinct frequency bands with stable radiation patterns and consistent gain characteristics. The fabricated prototype demonstrated excellent agreement between simulated and measured results, validating the precision and effectiveness of the proposed design methodology.

In the fourth part, an inverted crossed bowtie-shaped Sierpinski fractal antenna was proposed and experimentally verified. The design was modeled and optimized through a Python-assisted HFSS scripting workflow, enabling efficient management of the antenna's intricate geometry. The antenna exhibited multiple resonances spanning from the lower to upper microwave bands, with enhanced impedance matching and additional frequency bands relative to conventional fractal configurations. These findings confirm its effectiveness for diverse applications, including television broadcasting, satellite communication, radar systems, wireless broadband, and Wi-Fi.

Overall, all the proposed compact microstrip antenna structures were thoroughly simulated, analyzed, fabricated, and benchmarked against existing works, demonstrating superior multiband performance, miniaturization, and high gain.

1.1 Conclusions

In this thesis, an extensive investigation into the design, optimization, and experimental verification of compact multiband microstrip antennas employing fractal geometries has been conducted. The proposed antenna configurations are developed to address the increasing requirements of modern wireless and radar communication systems for compact structures that deliver high gain and broad multiband performance. The research integrates conventional microstrip theory with advanced fractal concepts, artificial intelligence, and automated optimization methods to enhance antenna efficiency and operational versatility.

The first proposed antenna features a hybrid wheel-shaped patch that integrates Sierpinski carpet and Koch snowflake fractal geometries. This configuration achieves five resonant frequencies at 2.45 GHz, 3.43 GHz, 7.69 GHz, 8.25 GHz, and 9.79 GHz, with return loss values reaching –24.24 dB, a VSWR below 1.13, and bandwidths ranging from 86 MHz to 202 MHz. The antenna attains a measured peak gain of 29.88 dBi and demonstrates stable radiation behavior, making it well-suited for Wi-Fi, 5G, radar, satellite, and Bluetooth communication systems.

To enhance the electromagnetic performance of complex fractal structures, an artificial neural network (ANN)-based optimization approach was developed for a modified Apollonian gasket antenna. The ANN model, trained with a limited dataset, successfully predicted the real and imaginary components of return loss with high accuracy and rapid convergence. The optimized antenna, operating between 7.4 GHz and 9.8 GHz, demonstrated significant improvement in impedance matching and return loss, validating the potential of AI-driven optimization in antenna design.

The subsequent contribution presented the design and realization of a compact rectangular nested fractal antenna intended for wide multiband applications. The structure incorporates a multilevel fractal slot arrangement, yielding resonances at 1.99, 3.68, 4.91, 6.11, 7.60, 8.06, and 9.39 GHz, with bandwidths ranging from 22 MHz to 210 MHz and a peak gain of 18.86 dBi, the fabricated prototype realized on an FR4 substrate of dimensions $40 \times 50 \times 0.8$ mm^3 exhibited excellent agreement between simulated and measured results, confirming the reliability and accuracy of the proposed design.

The research also introduced and experimentally validated a novel inverted crossed bowtie-shaped Sierpinski fractal antenna, representing an unexplored direction in fractal antenna design. The antenna was modeled and optimized using a Python-assisted HFSS scripting technique to efficiently handle its complex geometry. Constructed on an FR4 substrate with a dielectric constant of approximately 4.4, a thickness of 1.6 mm, and a loss tangent of 0.025, the proposed antenna exhibits resonances at 0.73, 2.75, 3.53, 5.22, and 5.64 GHz. These resonant frequencies encompass various practical applications, such as television broadcasting, satellite links, radar operations, wireless broadband, and Wi-Fi communication. The comparative evaluation demonstrated enhanced impedance matching and the emergence of additional operating bands relative to conventional fractal designs. Furthermore, the close agreement between simulated and measured outcomes validates the precision and reliability of the proposed antenna configuration.

In summary, the findings of this study demonstrate that the proposed fractal-inspired antenna designs exhibit compact dimensions, high efficiency, and the ability to operate across multiple frequency bands while maintaining strong gain and stable radiation performance. The integration of fractal geometry, artificial intelligence, and automated design tools provides a powerful framework for future development of intelligent and reconfigurable antennas tailored for next-generation wireless communication systems.

1.2 Suggestions for Further Work

The swift advancement of wireless communication technologies has created an increasing need for compact, high-gain, and multiband antennas. Consequently, additional enhancements to antenna structures are required. The following points outline potential avenues for future research derived from the findings presented in this thesis:

- Investigate novel methods for antenna miniaturization using more advanced fractal geometries or hybrid miniaturization strategies to meet the requirements of ultra-compact platforms.
- Enhance the gain and radiative performance of compact antenna structures using artificial magnetic conductors (AMCs), metasurfaces, or metamaterial-inspired superstrates.
- Study the use of the proposed fractal designs in MIMO systems, focusing on mutual coupling reduction, isolation enhancement, and diversity

performance.

- Develop flexible or wearable versions of the antennas using textile or polymer-based substrates for body-worn or implantable communication systems.
- Expand the ANN-based optimization model into deeper architectures, such as convolutional neural networks or reinforcement learning, for dynamic reconfigurability and intelligent antenna adaptation.
- Integrate the proposed antenna elements into reconfigurable intelligent surfaces (RIS) for smart propagation control and dynamic beam steering in 6G wireless networks.

The findings of this thesis form a solid basis for future advancements in intelligent, compact, and wideband antenna designs for high-performance wireless applications.

Author's publication list

Journal Publications

A- Category

[1] A. Azzouz, R. Bouhmidi, M. E. Munir, M. M. Nasralla, and M. Chetioui, "Characterization and analysis of hybrid fractal antennas for multiband communication and radar applications," *Fractal and Fractional*, vol. 10, no. 1, p. 47, 2026. https://doi.org/10.3390/fractalfract10010047

[2] A. Azzouz, R. Bouhmidi, M. Chetioui, R. Berber, A. J. A. Al-Gburi, *et al.*, "Design and performance analysis of a fan-shaped fractal antenna for radar systems and satellite communications," *Journal of Optoelectronics and Advanced Materials*, vol. 28, pp. 20–30, 2026. https://joam.inoe.ro/articles/design-and-performance-analysis-of-a-fan-shaped-fractal-antenna-for-radar-systems-and-satellite-communications/

B- Category

[3] A. Azzouz, R. Bouhmidi, M. E. Munir, M. M. Nasralla, and M. Chetioui, "Performance analysis of a high-gain multi-band wheel-shaped fractal antenna using Sierpinski carpet and Koch snowflake geometries," *Results in Engineering*, vol. 26, p. 105328, 2025. https://doi.org/10.1016/j.rineng.2025.105328

[4] A. Azzouz, R. Bouhmidi, M. Chetioui, R. Berber, and A. J. A. Al-Gburi, “Performance optimization of crossed bowties of inverted Sierpinski fractal antenna for multiband wireless communication applications,” *Telematics and Informatics Reports*, p. 100231, 2025. https://doi.org/10.1016/j.teler.2025.100231

[5] A. Azzouz, R. Bouhmidi, M. Chetioui, R. Berber, and A. J. A. Al-Gburi, “Design and experimental validation of a hybrid Koch–Minkowski fractal antenna for multiband wireless applications,” *SN Computer Science*, vol. 7, no. 4, p. 351, 2026. https://doi.org/10.1007/s42979-026-04781-4

[6] A. Azzouz, R. Bouhmidi, and M. Chetioui, “Performance optimisation of modified multiband Apollonian gasket fractal antenna using artificial neural network,” *Microwave Review*, vol. 30, no. 2, pp. 54–59, 2024. https://doi.org/10.18485/mtts$_{m}r$.2024.30.2.7

[7] A. Azzouz, R. Bouhmidi, M. Chetioui, R. Berber, and A. J. A. Al-Gburi, “Performance analysis of a rectangular nested fractal antenna for multiband applications,” *International Journal of Microwave & Optical Technology*, vol. 20, no. 2, 2025. https://www.ijmot.com/VOL-20-NO-2.aspx

International Conferences

IEEE-indexed international conferences

[1] A. Azzouz, R. Bouhmidi, M. E. Munir, M. Sheraz, T. C. Chuah,

and M. B. Roslee, “Optimized multiband fractal antenna design through advanced visual basic scripting and genetic algorithm,” in *Proc. 2024 Multimedia University Engineering Conference (MECON)*, pp. 1–5, 2024. https://doi.org/10.1109/MECON62796.2024.10776342

[2] A. Azzouz and R. Bouhmidi, “Recent advances and state of the art of multiband fractal antennas,” in *Proc. 2024 2nd International Conference on Electrical Engineering and Automatic Control (ICEEAC)*, pp. 1–5, 2024. https://doi.org/10.1109/ICEEAC61226.2024.10576389

[3] A. Azzouz, R. Bouhmidi, M. E. Munir, M. Sheraz, T. C. Chuah, and I. E. Lee, “Coaxial-fed crossed bowtie Sierpinski fractal multiband antenna design and analysis,” in *Proc. 2025 Multimedia University Engineering Conference (MECON)*, pp. 1–6, 2025. https://doi.org/10.1109/MECON67253.2025.11277142

Other international and national conferences

[4] Azzouz, A., Bouhmidi, R. and Khelil, A., 2023. Design and performance analysis of a high-gain coaxial probe-fed fractal antenna for multiband applications using Sierpinski triangle geometry. In: Proceedings of the 1’st International Conference on Advances in Electronics, Control and Computer Technologies (ICAECCT’23), Mascara, Algeria.

[5] Bouhmidi, R., Chetioui, M., Azzouz, A., Damou, M., Boudkhil, A. and Bouras, B., 2023. Sierpinski carpet fractal antenna design using HFSS scripting

tool. In: Proceedings of the 4th International Conference on Technological Advances in Electrical Engineering (ICTAEE'23), Skikda, Algeria.

[6] Azzouz, A., Bouhmidi, R. and Chetioui, M., 2024. Design of a triple-band high-gain fractal MIMO antenna with low ECC for satellite and radar systems. In: Proceedings of the 1'st National Conference of Advanced Systems in Electrical Engineering (NCASEE'24), University M'Hamed Bougara of Boumerdes, Boumerdes, Algeria.

[7] Azzouz, A., Bouhmidi, R. and Chetioui, M., 2024. Return loss enhancement of microstrip fractal antenna using artificial neural networks. In: Proceedings of the National Conference on Artificial Intelligence in Electrical Engineering (NCAIEE'24), Medea, Algeria.

References

[1] Priyanka Saxena, Prabal Bhatnagar, and Umesh Gupta. "Design and analysis of CMOS microstrip antenna using MATLAB". In: *International Journal of Computer Applications* 149.10 (2016).

[2] ML Liya and VM Jayakrishnan. "Enhancement techniques in microstrip patch antenna-a brief review". In: *2022 3rd International Conference on Electronics and Sustainable Communication Systems (ICESC)*. IEEE. 2022, pp. 367–371.

[3] Akram El Hamdouni et al. "A Comparison Between the Microstrip and the Co-Planar Wave-Guide Antennas in Ultra-Wide-Band Applications by Using Fractal Geometry". In: *Emerging Innovations in Microwave and Antenna Engineering*. IGI Global Scientific Publishing, 2019, pp. 258–289.

[4] Osman Diriye Hussein and Anisa Ali Hussein. "Design of microstrip patch antenna for radar and 5G applications". In: *ESP Journal of Engineering & Technology Advancements* 3.2 (2023), pp. 7–19.

[5] Mulugeta T Gemeda and Kinde A Fante. "Inset-Feed Rectangular Microstrip Patch Antenna Array Performance Enhancement for 5G Mobile Applications". In: *International Conference on Advances of Science and Technology*. Springer. 2020, pp. 284–303.

[6] RV Durga et al. "Design, Implementation and Machine Learning Analysis of Frequency Reconfigurable Microstrip Antenna for Defense Applications". In: *2022 International Conference on Sustainable Computing and Data Communication Systems (ICSCDS)*. IEEE. 2022, pp. 926–931.

[7] ADNAN SONDAŞ and Mustafa Hikmet Bilgehan Ucar. "An implantable microstrip antenna design for MICS-band biomedical applications". In: *Turkish Journal of Electrical Engineering and Computer Sciences* 24.4 (2016), pp. 2267–2273.

[8] Sadman Ishraq et al. "Implantable UWB Microstrip Patch Antenna for Biomedical Applications". In: *2024 International Conference on Sustainable Communication Networks and Application (ICSCNA)*. IEEE. 2024, pp. 327–332.

[9] Constantine A Balanis. *Antenna theory: analysis and design*. John wiley & sons, 2016.

[10] Kebonyethebe Ramahatla et al. "Multiband reconfigurable antennas for 5G wireless and CubeSat applications: A review". In: *IEEE Access* 10 (2022), pp. 40910–40931.

[11] Navneet Kumar and Narinder Sharma. "The various feeding techniques of microstrip patch antenna using HFSS". In: *SSRG International Journal of Electronics and Communication Engineering* 6.6 (2019), pp. 23–29.

[12] Sakshi Singh and Jitesh Kumar. "A review paper on rectangular microstrip patch antenna". In: *National Conference on Industry 4.0 (NCI-4.0)*. 2020.

[13] TV Padmavathy, M Dinesh Kumar, and L Joy Jason. "Design of quad slot microstrip patch antenna with edge feed for WiMAX applications". In: *IET Chennai Fourth International Conference on Sustainable Energy and Intelligent Systems (SEISCON 2013)*. IET. 2013, pp. 421–425.

[14] Rozh Najeeb et al. "Design and simulation of microstrip patch antenna array for X-Band applications". In: *2016 HONET-ICT*. IEEE. 2016, pp. 79–83.

[15] Mehr e Munir, Khalid Mahmood, and Saad Hassan Kiani. “E-shape Multiband Patch Antenna for 4G, C-band and S-band Applications”. In: *International Journal of Advanced Computer Science and Applications* 9.5 (2018).

[16] David M Pozar. “Microstrip antenna aperture-coupled to a microstripline”. In: *Electronics letters* 21.2 (1985), pp. 49–50.

[17] AC Buck and DM Pozar. “Aperture-coupled microstrip antenna with a perpendicular feed”. In: *Electronics letters* 22.3 (1986), pp. 125–126.

[18] PR Haddad and DM Pozar. “Characterisation of aperture coupled microstrip patch antenna with thick ground plane”. In: *Electronics Letters* 30.14 (1994), pp. 1106–1107.

[19] Anupam Kumar Yadav, Sandeep Singh, and Suman Lata Dhar. “Tri-Shul Shaped microstrip patch antenna for X-band wireless applications”. In: *International Journal of Scientific Research in Engineering and Management, ISSN* (2022), pp. 2582–3930.

[20] Reenu Tresa Jacob et al. “Feed Analysis of a Proximity Coupled Microstrip Patch Antenna”. In: *2022 IEEE International Symposium on Antennas and Propagation and USNC-URSI Radio Science Meeting (AP-S/URSI)*. IEEE. 2022, pp. 846–847.

[21] Nafati Aboserwal et al. “An accurate analytical model to calculate the impedance bandwidth of a proximity coupled microstrip patch antenna (PC-MSPA)”. In: *IEEE Access* 8 (2020), pp. 41784–41793.

[22] Bhupendra Pratap Singh, Saurabh Singh, and Anand Kumar Sharma. “DESIGN OF MULTISTANDARD FRACTAL AND PLANAR ANTENNAS IN MIMO CONFIGURTATION FOR HANDHELD TERMINAL APPLICATIONS”. In: (2016).

[23] Amar Sharma et al. “A CPW-fed structure shaped substrate wideband microstrip antenna for wireless applications”. In: *Journal of Microwaves, Optoelectronics and Electromagnetic Applications* 16 (2017), pp. 419–433.

[24] T Lakshmi Narayana, K Girija Sravani, and K Srinivasa Rao. “Design and analysis of CPW based shunt capacitive RF MEMS switch”. In: *Cogent Engineering* 4.1 (2017), p. 1363356.

[25] Kezia Noviani Anou et al. “Perancangan Dan Karakterisasi Antena Monopole Sebagai Pemancar Dan Penerima Gelombang Wifi Frekuensi 2, 4 GHz”. In: *Jurnal natural* 15.1 (2019), pp. 39–45.

[26] Keith Carver and James Mink. “Microstrip antenna technology”. In: *IEEE transactions on antennas and propagation* 29.1 (1981), pp. 2–24.

[27] Miloslav Capek and Lukas Jelinek. “The upper bound on antenna gain and its feasibility as a sum of characteristic gains”. In: *IEEE Transactions on Antennas and Propagation* 72.1 (2023), pp. 277–289.

[28] Ben AP Nel, Anja K Skrivervik, and Mats Gustafsson. “Radiation efficiency and gain bounds for microstrip patch antennas”. In: *IEEE Transactions on Antennas and Propagation* (2024).

[29] Vinay B Ramakrishnaiah, Robert F Kubichek, and Suresh S Muknahallipatna. “Correction factor for power gain in antenna arrays”. In: *International Journal of Communications, Network and System Sciences* 11.3 (2018), pp. 45–52.

[30] Ranga Rodrigo. “Fundamental parameters of antennas”. In: *Dostupné na internete: https://www. ent. mrt. ac. lk/˜ ranga/courses/en4620_2010 L* 2 (2010).

[31] Chi-Chih Chen and JL Volakis. “Ultrawide bandwidth antenna design”. In: *Antenna engineering handbook* 4 (2007).

[32] Georges A Deschamps. “Microstrip microwave antennas”. In: *Proceedings of the Third Symposium on the USAF Antenna Research and Development Program, Oct.* 1953, pp. 18–22.

[33] Douglas H Werner and Suman Ganguly. “An overview of fractal antenna engineering research”. In: *IEEE Antennas and propagation Magazine* 45.1 (2003), pp. 38–57.

[34] Xiaobo Huang, Xuewei Lv, and Zhengliang Xue. “Interpretation on iron ore granulation process based on particle-size analysis”. In: *ISIJ International* 56.11 (2016), pp. 1964–1972.

[35] David Gala et al. “Miniature microstrip patch antenna loaded with a space-filling transmission line based on the fractal Hilbert curve”. In: *Microwave and Optical Technology Letters* 38.4 (2003), pp. 311–312.

[36] Ethan Allan Davis. “On the wetting states of low melting point metal Galinstan and wetting characteristics of 3-dimensional nanostructured fractal surfaces”. In: (2017).

[37] Steven R Best. “On the significance of self-similar fractal geometry in determining the multiband behavior of the Sierpinski gasket antenna”. In: *IEEE antennas and wireless propagation letters* 1 (2005), pp. 22–25.

[38] Hui-Hui Ding et al. “Phylogeny and character evolution of the fern genus Tectaria (Tectariaceae) in the Old World inferred from chloroplast DNA sequences”. In: *Molecular Phylogenetics and evolution* 80 (2014), pp. 66–78.

[39] Jaume Anguera et al. “Fractal antennas: An historical perspective”. In: *Fractal and Fractional* 4.1 (2020), p. 3.

[40] Susilo Ady Saputro and Jae-Young Chung. “Hilbert curve fractal antenna for dual on-and off-body communication”. In: *Progress In Electromagnetics Research Letters* 58 (2016), pp. 81–88.

[41] David Auber, Noel Novelli, and Guy Melançon. “Visually mining the datacube using a pixel-oriented technique”. In: *2007 11th International Conference Information Visualization (IV’07)*. IEEE. 2007, pp. 3–10.

[42] HV Koch. “Sur une courbe continue sans tangente, obtenue par une construction géométrique élémentaire”. In: *Arkiv for Matematik, Astronomi och Fysik* 1 (1904), pp. 681–704.

[43] Atif Jamil et al. “Design and Geometric Transformations of Koch Curve Monopole Antennas”. In: *Engineering, Technology & Applied Science Research* 12.2 (2022), pp. 8452–8457.

[44] Kosala Dwidja Purnomo, Siti Fatimah, and Bagus Juliyanto. “Generation of Fractal Objects with Iterated Function System on the Developments of Trellis Ornament Designs”. In: *BERKALA SAINSTEK* 13.1 (2025), pp. 1–7.

[45] Georg Cantor. “Ueber unendliche, lineare Punktmannichfaltigkeiten”. In: *Mathematische Annalen* 21.4 (1883), pp. 545–591.

[46] Jaume Anguera et al. “Fractal shaped antennas: A review”. In: *Encyclopedia of RF and microwave engineering* (2005).

[47] Carles Puente Baliarda et al. “Fractal multiband antenna based on the Sierpinski gasket”. In: *Electronics Letters* 32.1 (1996), pp. 1–2.

[48] CTP Song et al. “Sierpinski monopole antenna with controlled band spacing and input impedance”. In: *Electronics Letters* 35.13 (1999), pp. 1036–1037.

[49] George F Tsachtsiris et al. “Analysis of a modified Sierpinski gasket monopole antenna printed on dual band wireless devices”. In: *IEEE transactions on antennas and propagation* 52.10 (2004), pp. 2571–2579.

[50] Carles Puente-Baliarda et al. “On the behavior of the Sierpinski multiband fractal antenna”. In: *IEEE Transactions on Antennas and propagation* 46.4 (2002), pp. 517–524.

[51] Ademola O Kaka et al. “Modified Hilbert fractal geometry, multi-service, miniaturized patch antenna for UWB wireless communication”. In: *COMPEL-The*

international journal for computation and mathematics in electrical and electronic engineering 31.6 (2012), pp. 1835–1849.

[52] Jingming Zheng et al. “A CP antenna of wide half-power beamwidth for UHF RFID near-and far-field applications”. In: *Progress In Electromagnetics Research Letters* 72 (2018), pp. 61–67.

[53] Utsab Banerjee, Anirban Karmakar, and Anuradha Saha. “A review on circularly polarized antennas, trends and advances”. In: *International Journal of Microwave and Wireless Technologies* 12.9 (2020), pp. 922–943.

[54] Constantine A Balanis. *Antenna theory: analysis and design*. John wiley & sons, 2016.

[55] Anirban Karmakar. “Fractal antennas and arrays: A review and recent developments”. In: *International Journal of Microwave and Wireless Technologies* 13.2 (2021), pp. 173–197.

[56] Amrita Rai et al. “Design, Simulation and Comparative Analysis of Wideband & Multiband Fractal Antenna for 5G and Wireless Application”. In: *2024 11th International Conference on Reliability, Infocom Technologies and Optimization (Trends and Future Directions)(ICRITO)*. IEEE. 2024, pp. 1–6.

[57] Mohamad Yafik Ihtisyam Yazid et al. “A sierpinski arrowhead curve slot vivaldi antenna for microwave head imaging system”. In: *IEEE Access* 11 (2023), pp. 32335–32347.

[58] R Kalaiyarasan, G Nagarajan, and R Senthil Kumaran. “Design and Implementation of an Efficient Sierpinski Carpet Fractal Antenna for 2.45 GHZ Applications”. In: *SN Computer Science* 4.6 (2023), p. 728.

[59] Dilaawaiz Fazal, Qasim Umar Khan, and Ic-Pyo Hong. “Multiband antenna design with enhanced radiations using characteristic mode analysis”. In: *Scientific Reports* 13.1 (2023), p. 17829.

[60] Neeraj Rao. "Modified sierpinski and its use in fractal patch antenna for miniaturization and multiband behavior". In: *2022 IEEE Microwaves, Antennas, and Propagation Conference (MAPCON)*. IEEE. 2022, pp. 1804–1809.

[61] Said Benaissa et al. "Design and experimental validation of a multiband conformal patch antenna for animal-ingestible bolus applications". In: *IEEE Transactions on Antennas and Propagation* 71.8 (2023), pp. 6365–6377.

[62] Abdelbasset Azzouz et al. "Performance Analysis of a High-Gain Multi-Band Wheel-Shaped Fractal Antenna Using Sierpinski Carpet and Koch Snowflake Geometries". In: *Results in Engineering* (2025), p. 105328.

[63] Haizhuo He et al. "A microstrip patch antenna design based on ANN". In: *2021 International Symposium on Antennas and Propagation (ISAP)*. IEEE. 2021, pp. 1–2.

[64] Jing Rui Wang, Wen Jie Liu, and Mei Song Tong. "An artificial neural network based design of triple-band microstrip patch antenna for WLAN applications". In: *2020 IEEE MTT-S International Conference on Numerical Electromagnetic and Multiphysics Modeling and Optimization (NEMO)*. IEEE. 2020, pp. 1–4.

[65] Francismari Noronha dos Santos et al. "Analysis and design of microstrip antennas by Artificial Neural Networks". In: *2011 SBMO/IEEE MTT-S International Microwave and Optoelectronics Conference (IMOC 2011)*. IEEE. 2011, pp. 226–230.

[66] Aarti Gehani, Dhaval Pujara, and Dipak Adhyaru. "Analysis of an elliptical patch antenna using artificial neural networks". In: *2012 IEEE Asia-Pacific Conference on Antennas and Propagation*. IEEE. 2012, pp. 157–158.

[67] Hemraj Kumawat and Poonam Agarwal. "Artificial Neural Network Model to Predict the Design Parameters of Inset-fed Microstrip Patch Antenna". In: *2021 8th International Conference on Signal Processing and Integrated Networks (SPIN)*. IEEE. 2021, pp. 943–948.

[68] Ivan Vilovic and Niksa Burum. “Design and feed position estimation for circular microstrip antenna based on neural network model”. In: *2012 6th European Conference on Antennas and Propagation (EUCAP)*. IEEE. 2012, pp. 3614–3617.

[69] Ijaz Khan et al. “Design annular ring microstrip antenna based on artificial neural network”. In: *2018 2nd IEEE Advanced Information Management, Communicates, Electronic and Automation Control Conference (IMCEC)*. IEEE. 2018, pp. 2033–2037.

[70] Bishal Dey Sarkar et al. “Resonant frequency determination of rectangular patch antenna using Neural Network”. In: *2015 1st International conference on next generation computing technologies (NGCT)*. IEEE. 2015, pp. 915–917.

[71] Balwinder Singh Dhaliwal and Shyam S Pattnaik. “Performance evaluation of artificial neural networks in microstrip fractal antenna parameter estimation”. In: *2012 IEEE International Conference on Communication Systems (ICCS)*. IEEE. 2012, pp. 135–139.

[72] Jayshree Das et al. “RBF-Neural Network Based Implementation of Sierpinski Carpet Shaped Fractal Antenna”. In: *2023 IEEE 3rd International Conference on Technology, Engineering, Management for Societal impact using Marketing, Entrepreneurship and Talent (TEMSMET)*. IEEE. 2023, pp. 1–5.

[73] Jing Jin et al. “Recent advances in neural network-based inverse modeling techniques for microwave applications”. In: *International Journal of Numerical Modelling: Electronic Networks, Devices and Fields* 33.6 (2020), e2732.

[74] Abdelbasset Azzouz, Rachid Bouhmidi, and Mohammed Chetioui. “Performance optimisation of modified multiband apollonian gasket fractal antenna using artificial neural network”. In: *Microwave Review* 30.2 (2024), pp. 54–59.

[75] Ramesh Kumar Verma and DK Srivastava. "Design and analysis of triple-band rectangular microstrip antenna loaded with notches and slots for wireless applications". In: *Wireless Personal Communications* 114.2 (2020), pp. 1847–1864.

[76] Oscar Ossa-Molina and Francisco López-Giraldo. "A simple model to compute the characteristic parameters of a slotted rectangular microstrip patch antenna". In: *Electronics* 11.1 (2022), p. 129.

[77] Andrea Martínez-Lozano et al. "UWB-printed rectangular-based monopole antenna for biological tissue analysis". In: *Electronics* 10.3 (2021), p. 304.

[78] Anuradha A Palsokar and SL Lahudkar. "Frequency and pattern reconfigurable rectangular patch antenna using single PIN diode". In: *AEU-International Journal of Electronics and Communications* 125 (2020), p. 153370.

[79] Said Douhi et al. "Design of a flexible rectangular antenna array with high gain for RF energy harvesting and wearable devices". In: (2023).

[80] Abdelbasset Azzouz et al. "Performance Analysis of a Rectangular Nested Fractal Antenna for Multiband Applications." In: *International Journal of Microwave & Optical Technology* 20.2 (2025).

[81] William Clower et al. "Additive manufactured graphene composite Sierpinski gasket tetrahedral antenna for wideband multi-frequency applications". In: *Additive Manufacturing* 32 (2020), p. 101024.

[82] Iqra Masroor et al. "Sierpinski-carpet fractal frequency reconfigurable microstrip patch antenna design for ku/k/Ka band application". In: *Progress In Electromagnetics Research M* 106 (2021), pp. 59–69.

[83] Sarthak Singhal. "Asymmetrically CPW fed square Sierpinski Carpet ultra wideband terahertz antenna". In: *Optik* 242 (2021), p. 167056.

[84] DALIA AHMED AL-KHAFAF and JAFAR RAMADHAN MOHAMMED. "PERFORMANCE COMPARISON INVESTIGATION OF THE WIDEBAND AND FRACTAL MULTIBAND BOWTIE ANTENNAS". In: *Journal of Engineering Science and Technology* 19.3 (2024), pp. 966–976.

[85] Sanish Vaipel Sanu et al. "Fractal-enhanced microstrip antennas: miniaturization, multiband performance and cross-polarization minimization for Wi-Fi applications". In: *Engineering Proceedings* 59.1 (2023), p. 127.

[86] Deepanshu Kaushal and Rajeevan Chandel. "A proposal, design, and analysis of planar feed gasket antennas with modified substrate for multiband vehicular applications". In: *IETE Technical Review* 40.2 (2023), pp. 268–283.

[87] S Malathi, Subrajith Pradhan, and K Srinivasa Naik. "Modified Sierpinski Gasket Monopole Fractal Antenna for Sub 6 GHz 5G Applications". In: *Smart and Sustainable Technologies: Rural and Tribal Development Using IoT and Cloud Computing: Proceedings of ICSST 2021*. Springer, 2022, pp. 127–135.

[88] Abdelbasset Azzouz et al. "Performance optimization of crossed bowties of inverted Sierpinski fractal antenna for multiband wireless communication applications". In: *Telematics and Informatics Reports* (2025), p. 100231.

[89] Neeraj Rao. "Modified sierpinski and its use in fractal patch antenna for miniaturization and multiband behavior". In: *2022 IEEE Microwaves, Antennas, and Propagation Conference (MAPCON)*. IEEE. 2022, pp. 1804–1809.